JGR Atmospheres

RESEARCH ARTICLE
10.1029/2023JD040026

Key Points:

- A new melting model is proposed and introduced into forward operators for simulation of polarimetric radar data
- More reasonable polarimetric signatures of the melting layer are simulated using different double-moment microphysics schemes
- These polarimetric forward operators have potential to be used in data assimilation for improving high-resolution severe weather forecasts

Supporting Information:

Supporting Information may be found in the online version of this article.

Correspondence to:
P. Liu,
Peng.Liu-1@ou.edu

Citation:

Liu, P., Zhang, G., Carlin, J. T., & Gao, J. (2024). A new melting model and its implementation in parameterized forward operators for polarimetric radar data simulation with double moment microphysics schemes. *Journal of Geophysical Research: Atmospheres*, *129*, e2023JD040026. https://doi.org/10.1029/2023JD040026

Received 27 SEP 2023
Accepted 15 APR 2024

Author Contributions:

Conceptualization: Peng Liu, Guifu Zhang
Investigation: Peng Liu, Jacob T. Carlin, Jidong Gao
Methodology: Peng Liu, Guifu Zhang, Jacob T. Carlin
Project administration: Guifu Zhang
Validation: Peng Liu
Visualization: Peng Liu
Writing – original draft: Peng Liu
Writing – review & editing: Peng Liu, Guifu Zhang, Jacob T. Carlin, Jidong Gao

A New Melting Model and Its Implementation in Parameterized Forward Operators for Polarimetric Radar Data Simulation With Double Moment Microphysics Schemes

Peng Liu[1,2], Guifu Zhang[1,2], Jacob T. Carlin[3,4], and Jidong Gao[4]

[1]School of Meteorology, University of Oklahoma, Norman, OK, USA, [2]Advanced Radar Research Center, University of Oklahoma, Norman, OK, USA, [3]Cooperative Institute for Severe and High-Impact Weather Research and Operations, University of Oklahoma, Norman, OK, USA, [4]NOAA/OAR National Severe Storms Laboratory, Norman, OK, USA

Abstract To improve short-term severe weather forecasts through assimilation of polarimetric radar data (PRD), the use of accurate and efficient forward operators for polarimetric radar variables is required. In this study, a new melting model is proposed to estimate the mixing ratio and number concentration of melting hydrometeor species and incorporated in a set of parameterized polarimetric radar forward operators. The new melting model depends only on the mixing ratio and number concentration of rain and ice species and is characterized by its independence from ambient temperature and its simplicity and ease of linearization. To assess the impact of this newly proposed melting model on the simulated polarimetric radar variables, a real mesoscale convective system is simulated using three double-moment microphysics schemes. Compared with the output of the original implementation of the parameterized forward operators (PFO_Old) that rely on an "old" melting model which only estimates the mixing ratio of the melting species, the updated implementation with the new melting model (PFO_New) that estimates both the mixing ratio and number concentration of melting species eliminates the very large mass/volume-weighted mean diameter (D_m) at the bottom of the melting layer and produces more reasonable melting layer signatures for all three double-moment microphysics schemes that more closely match the corresponding radar observations. This suggests that the new melting model has more reasonable implicit estimates of mixing ratios and number concentrations of melting hydrometeor species than the "old" melting model.

Plain Language Summary Weather radars can provide information about observed precipitation that can be used to improve weather forecast models. Making use of this information requires linking the radar observations with the variables these models predict in an efficient and accurate way. One of the most pronounced signatures in weather radar observations occurs as precipitation melts from ice into rain. However, current operational forecast models do not explicitly predict melting ice as a separate category of precipitation. Therefore, existing methods for comparing radar observations to forecast models use an empirical melting model to estimate the mass of melting ice and assume melting ice has the same concentration as the model-predicted dry ice. These assumptions result in a simulated radar melting layer signature that is unrealistically thick and low. In this study, a new melting model is proposed for estimating both the mass and concentration of melting ice, and its effects on simulated radar variables are evaluated for a severe thunderstorm case. For all of the microphysics schemes investigated, the newly proposed melting model results in improved simulations of the size of melting ice particles and simulated radar variables that are closer to those observed.

1. Introduction

Weather radar networks have been upgraded with dual-polarization capability in many countries and regions, transitioning from providing the three single-polarization radar variables of reflectivity factor (Z or Z_H), radial velocity (v_r), and spectrum width (σ_v), to six variables, including three additional polarimetric variables: differential reflectivity (Z_{DR}), cross-correlation coefficient (ρ_{hv}), and differential phase (Φ_{DP}) or specific differential phase (K_{DP}). Polarimetric radar data (PRD) contain rich information about cloud and precipitation microphysics, such as the size, shape, orientation, phase, and composition of hydrometeors (Picca et al., 2014; Zhang et al., 2019). PRD offer an unprecedented opportunity to expand the knowledge of cloud microphysics processes to improve microphysics parameterization (Chen et al., 2021; Jung et al., 2012; Kumjian & Ryzhkov, 2008; Wu et al., 2021; Zhang et al., 2001, 2006; Zhou et al., 2022). Furthermore, PRD can be used to improve model initialization through data assimilation methods (Carlin et al., 2017; Ding et al., 2022; Du et al., 2021; Jung, Xue, et al., 2008; Jung, Zhang, & Xue, 2008; Putnam et al., 2019, 2021; Zhu et al., 2020).

Whether using PRD to improve microphysics parameterization or assimilating PRD to provide initial conditions for NWP models, an accurate and efficient PRD simulator, also known as a forward observation operator in data assimilation terminology, is necessary to link the observed polarimetric radar variables with the model state variables. A number of polarimetric radar simulators have been developed and successful in reproducing observed polarimetric signatures such as Z_{DR} and K_{DP} columns, Z_{DR} arcs, and ρ_{hv} rings in convective storms (Augros et al., 2016; Dawson et al., 2014; Jung, Zhang, & Xue, 2008; Jung et al., 2010; Li et al., 2022; Matsui et al., 2019; Oue et al., 2020; Ryzhkov et al., 2011; Wolfensberger & Berne, 2018; Xie et al., 2021; Zhang et al., 2021).

Jung et al. (2010) developed a polarimetric radar forward operator that performs numerical integration of hydrometeor scattering amplitudes calculated with the T-matrix method. Dawson et al. (2014) made improvements to Jung et al.'s (2010) operator to better treat small-to-medium-sized wet graupel and hail particles and diagnose water fractions. This polarimetric radar operator has been validated and applied in idealized and real cases (Johnson et al., 2016; Putnam et al., 2017; Snyder et al., 2017a, 2017b). Ryzhkov et al. (2011) described a similar polarimetric radar forward operator that decreases computational time by employing closed-form Rayleigh formulas for small particles and T-matrix calculations for larger particles, while ensuring accurate calculations for melting water-coated particles by using two-layer scattering equations. Zeng et al. (2016) presented the Efficient Modular Volume scanning RADar Operator (EMVORADO) for simulating v_r and Z_{H} in the Consortium of Small-scale Modeling (COSMO) model. This was extended to include dual-polarization variables in the Bonn Polarimetric Radar forward Operator (B-PRO) based on the T-matrix method for calculating scattering amplitudes (Xie et al., 2021). Shrestha, Mendrok and Brunner (2022), Shrestha, Mendrok, Pejcic et al. (2022), and Shrestha, Tromel, et al. (2022) used the B-PRO to reproduce the polarimetric features observed in convective storms and stratiform events. Wolfensberger and Berne (2018) proposed a polarimetric radar forward operator for the COSMO model which allows estimation of the full Doppler spectrum. The scattering properties for dry and wet hydrometeors were pre-computed using the T-matrix method. Other polarimetric radar forward operators and simulators, such as the POLArimetric Radar Retrieval and Instrument Simulator (POLARRIS-f) (Matsui et al., 2019), and a polarimetric radar forward operator developed by Li et al. (2022) for use in the Weather Research and Forecasting (WRF) model, have been proposed but did not consider melting or mixed-phased particles.

The aforementioned numerical integration-based PRD operators have limitations for data assimilation systems due to their difficulty in linearization and computational expense. Given the pressing need for more efficient and compatible polarimetric observation operators, Zhang et al. (2021) developed a set of parameterized polarimetric radar forward operators and tested them for both idealized and real supercell cases. Du et al. (2021) assessed the performance of these parameterized forward operators in a variational assimilation system. In the case of an idealized supercell storm, the assimilation of PRD led to a reduction in the root mean square errors (RMSEs) of the model state variables at each analysis cycle. These parameterized forward operators, distinguished by their high computational efficiency and differentiability, have shown significant potential and advantages for PRD assimilation.

Many polarimetric signatures of stratiform precipitation and convective storms are dominated by melting or mixed-phase particles when they are present, especially melting snow, melting graupel, and melting hail (Kumjian et al., 2010; Romine et al., 2008; Wolfensberger et al., 2016). Whether it is the simulation or the assimilation of PRD, the effect produced by melting species needs to be taken into account by the MP schemes or forward operator. Unfortunately, most single-moment (SM) bulk microphysics (MP) schemes that predict hydrometeor mixing ratios (q) and double-moment (DM) MP schemes that predict both q and total number concentration (N_t) that are widely used in operational forecasting systems fail to simulate melting hydrometeors. Over the last decade, several newly developed MP schemes, such as The Predicted Particle Properties (P3) and the Ice-Spheroids Habit Model with Aspect-Ratio Evolution (ISHMAEL) schemes, have removed the use of predefined categories and utilized the property-based approach to represent ice-phase species (Cholette et al., 2023; Jensen et al., 2017; Milbrandt et al., 2021; Morrison & Milbrandt, 2015). In particular, the P3 scheme has made noteworthy progress in simulating characteristics of mixed-phase particles and is used in the Global Environmental Multiscale model, which is an operational NWP model with a horizontal grid spacing of approximately 2.5 km (Cholette et al., 2023; Girard et al., 2014). However, when the results of typical SM or DM MP schemes are used as input to operators, melting particles need to be generated by a melting model and included/parameterized in the polarimetric radar forward operators in order to properly simulate the effects of mixed-phase particles on the polarimetric variables. Herein, the melting model refers to the one in the forward operator, which is different than the melting parameterization internal to each MP scheme.

Jung, Zhang, and Xue (2008) introduced a melting model to account for the presence of melting ice particles by assuming mixed-phase particles to exist only when rain and dry ice species coexist and redistributing the mixing ratios of the rain and dry species to form the mixed-phase species. This melting model was used in Zhang et al. (2021) for PRD simulations. However, Jung, Zhang, and Xue (2008) assumed the N_t of the melting species to be that of the corresponding dry species. This treatment of N_t was a problematic assumption and could introduce a substantial error when simulating polarimetric radar variables. Blahak (2016) proposed a melting model wherein the degree of melting (i.e., melted mass fraction) of particles is estimated as a function of particle size and ambient temperature. This melting model was introduced into EMVORADO and inherited by B-PRO. This melting model is good for characterizing stratiform precipitation, but there will be some issues in deep convection where strong updrafts may carry already melted particles above the fixed ambient temperature level (0°C or slightly below) where melting is assumed to start. Wolfensberger and Berne (2018) presented a melting model to estimate the mass concentrations and particles size distributions for melting species. However, the complex estimation process in this melting model is difficult to linearize and introduces limitations if applied to assimilation systems.

Motivated by the goal of achieving a polarimetric radar forward operator for representing melting species that is accurate, efficient, differentiable, and compatible with various SM/DM MP schemes, this paper proposes a new melting model to estimate the q and N_t of melting species (melting snow, graupel, and hail) and investigates the impact of the estimated q and N_t of melting species on the simulation of polarimetric radar variables. In this study, the new melting model is applied to the parameterized operators developed by Zhang et al. (2021), although it is expected that the new melting model would also be compatible with other polarimetric radar forward operators. In general, DM MP schemes do a significantly better job reproducing polarimetric signatures and the evolution of convective storms compared to SM MP schemes (Jung et al., 2010, 2012; Putnam et al., 2014, 2017). However, the ice-phase categories predefined in different DM MP schemes have various physical properties, and different DM MP schemes show varying skill in replicating certain polarimetric signatures. Therefore, it is necessary to examine the applicability of the new melting model with parameterized polarimetric radar forward operators using different DM MP schemes. This study evaluates a real mesoscale convective system (MCS) case due to the presence of a pronounced melting layer signature in the MCS stratiform region.

This paper is organized as follows: Section 2 describes the selected case and radar data, the model configuration and MP schemes, and details of the melting model and parameterized operators. Section 3 presents the simulation results. Section 4 concludes with a summary and discussion.

2. Data and Methods

2.1. Case Overview and Radar Data

A frontal boundary positioned across northern Kansas and northern Missouri triggered the formation of multiple areas of severe thunderstorms during the afternoon and evening of 28 May 2019. As time progressed, these scattered thunderstorms advanced northeastward along the front, coalescing into several MCSs that stretched from eastern Iowa and northern Illinois down to northern Kansas. Persistent heavy rainfall resulted in numerous instances of flash flooding across southern Iowa. Widespread damage from strong winds and hail was also reported across southern Iowa, northern Missouri, and western Illinois (SPC, 2019).

All radar data is downloaded from the NEXRAD Level-II data repository at the National Centers for Environmental Information. The radar data is quality controlled, including the removal of radar ground clutter, non-meteorological reflectivity, and the removal of isolated gates. After quality control, radar variables are linearly interpolated onto the model grid. In the event that data from multiple radars exist at a model point, the polarimetric radar variables are selected from the radar which provided the largest reflectivity value.

2.2. Model Configuration

Following the Warn-on-Forecast (WoF) system's real-time settings (Stensrud et al., 2009, 2013), the WRF model version 3.7.1 (Skamarock et al., 2008) is employed to perform the numerical simulation. The horizontal domain is set at 601 × 601 grid points, with a horizontal grid spacing of 1.5 km, while the vertical dimension comprises 51 levels, extending up to the model top at 50 hPa. Initial fields and boundary conditions are from the 3.0-km High-Resolution Rapid Refresh (HRRR) forecast data, provided at 1-hr intervals. The WRF model was initialized at 1800 UTC on 28 May 2019, and free forecasts were conducted until 0200 UTC on 29 May without assimilating radar data. The extended free forecast period allows for the free development of MP processes like size sorting and avoids the influence of the data assimilation system on hydrometeors. The physics parameterization schemes include the Rapid Radiative Transfer Model for General Circulation Models (RRTMG) for both long-wave and short-wave radiation schemes (Iacono et al., 2008), as well as the Yonsei University Planetary Boundary-Layer physics scheme (Hong et al., 2006). No cumulus parameterization scheme is employed.

2.3. Microphysics Schemes

In WRF, the bulk MP schemes employ a three-parameter gamma distribution function to represent the cloud and precipitation particle size distributions (PSD):

$$N(D) = N_0 D^{\mu} e^{-\Lambda D}, \tag{1}$$

where D is the equivalent volume particle diameter and N_0, Λ, and μ are the intercept, slope, and shape parameters, respectively. Ignoring truncation effects, the nth moment of the PSD is:

$$M_n = \int_0^{\infty} D^n N(D)\, dD = N_0 \Lambda^{-(\mu+n+1)} \Gamma(\mu + n + 1). \tag{2}$$

In most SM MP schemes, N_0 is fixed and Λ varies based only on q during the forecast. In DM MP schemes, both N_0 and Λ are allowed to vary independently. The prognostic q and N_t are related to various moments of the PSD. The size distribution parameters N_0 and Λ can be derived from the predicted q and N_t using a fixed μ value for each species x, where $x \in [c, r, i, s, g, h]$ represents cloud droplets, rain, cloud ice, snow, graupel, and hail, respectively. This study utilizes three DM bulk MP schemes within the WRF model: the Milbrandt-Yau scheme (Milbrandt & Yau, 2005a, 2005b) (referred to as MY2), the Morrison scheme (Morrison et al., 2009) (referred to as MOR), and the National Severe Storms Laboratory scheme (Mansell et al., 2010) (referred to as NSSL).

The MY2 and NSSL schemes predict q and N_t for cloud droplets, cloud ice, rain, snow, graupel, and hail. In contrast, the MOR scheme predicts q and N_t for cloud droplets, cloud ice, rain, snow, and a single graupel-like rimed-ice species. For the precipitation species (rain, snow, graupel, and hail) as well as cloud ice, a fixed value of $\mu = 0$ is employed in both MY2 and MOR. For cloud droplets, MY2 uses a fixed $\mu = 1$ while MOR employs a variable μ associated with the predicted droplet N_t. The NSSL scheme employs $\mu = -0.8$ for snow and $\mu = 1$ for hail.

In the MY2 scheme, for all hydrometeor species except snow, the mass-diameter relationship follows $m(D) = c_x D^{d_x}$, with each species $c_x = (\pi/6)\rho_x$ and $d_x = 3$, where ρ_x is the bulk density of the particles of species x. The snow category uses $c_s = 0.1597$ and $d_s = 2.078$, implying a snow density that decreases with particle size. For cloud ice, graupel, and hail, fixed bulk densities of 500, 400, and 900 kg m^{-3} are used. The MOR scheme assumes a fixed snow density of 100 kg m^{-3}, while the density of other species is the same as in MY2. The NSSL scheme predicts the volume mixing ratio of graupel in addition to q and N_t. It assumes that snow and hail particles have bulk densities of 100 and 900 kg m^{-3}, respectively, and allows for a variable bulk graupel density. While there is a version of the MY2 that can also predict the bulk density of graupel (Milbrandt & Morrison, 2013), it is not currently incorporated into the WRF.

2.4. Parameterized Polarimetric Radar Forward Operators and Melting Model

2.4.1. Parameterized Polarimetric Radar Forward Operators (PFOs)

PFOs are a set of parameterized relations between the polarimetric radar variables and the model state parameters, which are derived through scattering calculations and fitting procedures. The PFOs used in this study were developed and documented in Zhang et al. (2021), which are summarized as follows.

For an exponential distribution, N_0 and Λ can be expressed in terms of the predicted model state variables of q, which is related to water content by $W_x = \rho_a q_x$ (g m^{-3}), and N_t, according to:

$$\Lambda_x = \left(\frac{\pi \rho_x N_{t,x}}{\rho_a q_x}\right)^{1/3}, \tag{3}$$

$$N_{0x} = \frac{\rho_a q_x {\Lambda_x}^4}{\pi \rho_x}. \tag{4}$$

The particle mass/volume-weighted mean diameter D_m (mm) can be defined using PSD moments as:

$$D_{m,x} \equiv \frac{M_{4x}}{M_{3x}} = \frac{4}{\Lambda_x} = 4\left(\frac{\rho_a q_x}{\pi \rho_x N_{t,x}}\right)^{1/3}, \tag{5}$$

$$Z_x \equiv M_{6x} = 11.25 \times 10^3 \frac{\rho_a q_x}{\pi \rho_x} {D_{m,x}}^3, \tag{6}$$

where the factor of 10^3 comes from the unit conversion as ρ_x is in g cm^{-3} while D_m in mm. For rain, using the T-matrix-calculated scattering amplitudes, polarimetric variables are calculated for a unit water content ($W_r = \rho_a q_r = 1$ g m^{-3}) and a set of D_m for exponentially distributed PSDs and an S-band radar wavelength of about 10.7 cm. The shape and orientation of hydrometeor particles, mean axis ratio, and standard deviation of the canting angles follow those documented in Zhang et al. (2021). The calculated polarimetric variables are then fitted to polynomial functions of D_m, as shown by Mahale et al. (2019). Compared to rain, the scattering amplitude calculations and parameterizations of ice and melting ice species are more complicated because of the increased variability in density during the melting stage and their irregular shapes, as well as the orientation of the particles. Zhang et al. (2021) expanded this fitting process to include ice and melting hydrometeor species. For a given melting species, the percentage of melting (f_{mx}), q, N_t, and density of the melting species (ρ_{mx}) were estimated in a melting model. Then, the D_m is calculated from Equation 5, and the corresponding polarimetric radar variables are parameterized as polynomial functions of D_m and f_{mx} as follows:

$$Z_h(x) \approx Z_x\left[a_{Z0}\left(f_{mx}\right) + a_{Z1}\left(f_{mx}\right)D_{m,x} + a_{Z2}\left(f_{mx}\right){D_{m,x}}^2 + a_{Z3}\left(f_{mx}\right){D_{m,x}}^3\right]^2, \tag{7}$$

$$Z_{dr}(x) \approx a_{d0}\left(f_{mx}\right) + a_{d1}\left(f_{mx}\right)D_{m,x} + a_{d2}\left(f_{mx}\right){D_{m,x}}^2, \tag{8}$$

$$K_\mathrm{DP}(x) \approx \rho_a q_x\left[a_{K0}\left(f_{mx}\right) + a_{K1}\left(f_{mx}\right)D_{m,x} + a_{K2}\left(f_{mx}\right){D_{m,x}}^2\right]/\rho_{mx}, \tag{9}$$

$$\rho_{hv}(x) \approx a_{\rho 0}\left(f_{mx}\right) + a_{\rho 1}\left(f_{mx}\right)D_{m,x} + a_{\rho 2}\left(f_{mx}\right){D_{m,x}}^2, \tag{10}$$

where Z_x is calculated from Equation 6. For melting ice particles, the fitting coefficients depend on the percentage of melting, so the calculation and fitting procedure is done for different percentages of melting. Then, the coefficients of the radar variables are further represented by a polynomial function of percentages of melting, as detailed in Tables 1–3 of Zhang et al. (2021). The polarimetric radar variables for all species are computed using Equations 9–12 from Mahale et al. (2019) for rain and Equations 7–10 above for all other species. Subsequently, the final variables for a grid box containing multiple species are obtained through summation across all species, following Equations 22–25 provided by Zhang et al. (2021).

2.4.2. The "Old" Melting Model and Its Implementation in PFOs

As previously mentioned, Jung, Zhang, and Xue (2008) introduced a melting model that takes out parts from rain and dry ice hydrometeors to construct a new melting ice species composed of water, ice, and/or air (i.e., a mixed-phase species). Within the melting model, the assumption is made that a mixed-phase species, such as melting snow, only exists when both rain and snow are present simultaneously. Then, an assumed fraction F_x is given as:

$$F_x = F_\mathrm{max}\left[\min\left(q_x/q_r, q_r/q_x\right)\right]^{0.3}, \tag{11}$$

where $x \in [s, g, h]$, and $F_{\max} = 0.5$ is set. The fraction F_x reaches a maximum when the rain q_r and ice particles mixing ratios q_x are equal and decreases to 0.0 when one of them vanishes. When fraction F_x is determined, the mass of rainwater ($q_{mx,r}$) and dry ice ($q_{mx,d}$) in the new mixed-phase species is given by $q_{mx,r} = F_x q_r$ and $q_{mx,d} = F_x q_x$, respectively. Consequently, the total q of this mixed-phase species, q_{mx}, is defined as:

$$q_{mx} = F_x\left(q_r + q_x\right). \tag{12}$$

To ensure the conservation of mass for the total amount of rain and ice, the q of rainwater in the mixed-phased species ($q_{mx,r}$) is subtracted from q_r to yield the q of pure rainwater (i.e., $q_{pr} = (1 - F_s - F_g - F_h)q_r$), and correspondingly, $q_{\mathrm{px}} = (1 - F_x)q_x$ for pure ice particles. In addition, the maximum value of F_x is fixed to ensure that q_{pr} will never be less than zero. The percentage of melting f_{mx} (also called the mass water faction) is given as:

$$f_{mx} = F_x q_r / F_x\left(q_r + q_x\right) = q_r / \left(q_r + q_x\right). \tag{13}$$

The density of the melting species, ρ_{mx}, is parameterized as:

$$\rho_{mx} = \rho_{dx}\left(1 - {f_{mx}}^2\right) + \rho_r {f_{mx}}^2, \tag{14}$$

where ρ_{dx} is the density of dry snow, hail, and graupel.

As described in Zhang et al. (2021), the original implementation of the parameterized forward operators (PFO_Old) utilizes Equations 12–14 in the "old" melting model of Jung, Zhang, and Xue (2008) to estimate the q of the melting species, the percentage of melting, and the density of the melting species, respectively, and uses the N_t of the dry ice species as the N_t of the melting species.

2.4.3. The New Melting Model and Its Implementation in PFOs

The present study proposes a new melting model to estimate the q and N_t of melting species based on the geometric mean of rain and dry species. In the new melting model, the total q and N_t of the melting species x are assumed as:

$$q_{mx} = \left(q_r q_x\right)^{½}, \tag{15}$$

$$N_{t,mx} = \left(N_{t,r} N_{t,x}\right)^{½}, \tag{16}$$

then, the q of water ($q_{mx,r}$) and dry ice ($q_{mx,d}$) within the melting species are defined as:

$$q_{mx,r} = q_{mx} f_{mx} = \frac{q_{mx} q_r}{\left(q_r + q_x\right)}, \tag{17}$$

$$q_{mx,d} = q_{mx}\left(1 - f_{mx}\right) = \frac{q_{mx} q_x}{\left(q_r + q_x\right)}. \tag{18}$$

As in the "old" melting model, the q of rain and ice in the melting species is removed from the predicted total q of rain and ice to ensure mass conservation (i.e., the q of pure rainwater is $q_{pr} = q_r - q_{ms,r} - q_{mg,r} - q_{mh,r}$ and the q of dry ice particles is $q_{px} = q_x - q_{mx,d}$). However, N_t is not conserved in a similar manner. The N_t of pure rainwater is $N_{t,pr} = N_{t,r}$, and the N_t of pure ice particles is $N_{t,px} = N_{t,x}$. Also, specifying a maximum proportion for $q_{mx,r}$ ensures that $q_{r,p}$ will not be less than zero. Figure 1 illustrates an example of the estimated q of the melting species using the "old" and new melting models, which shows a more continuous change near the middle of the melting layer where $q_r = q_x$ compared to the "old" melting model of Jung, Zhang, and Xue (2008).

In the updated implementation of the parameterized forward operators (PFO_New), Equations 15 and 16 in the new melting model are used to estimate q and N_t for the melting species, and Equations 13 and 14 are used, as with the "old" melting, to calculate the percentage of melting and density of the melting species. The D_{m} of melting

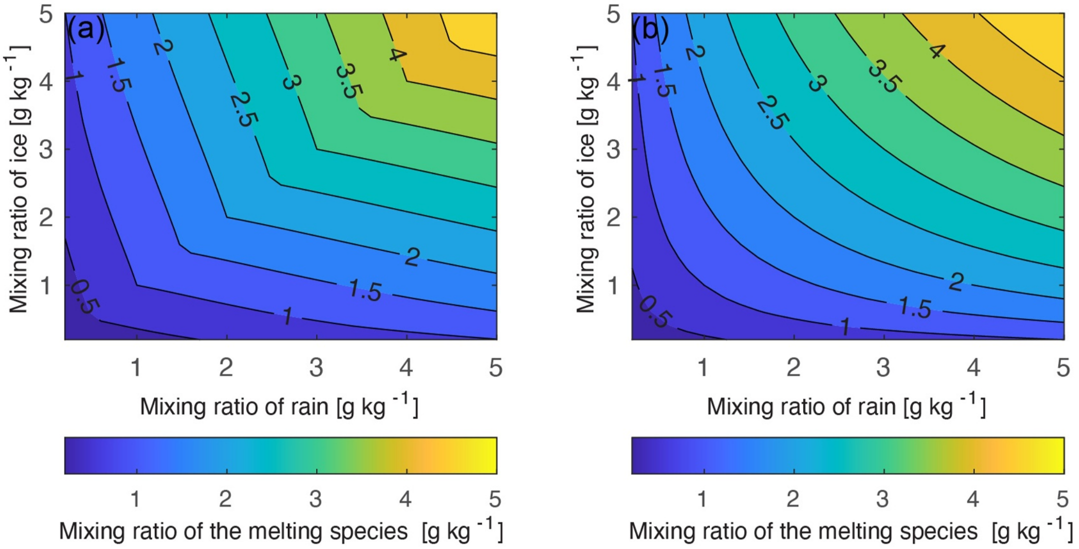

Figure 1. The estimated q of the melting ice particles using the q of rain (x-axis) and ice particles (y-axis) for (a) the "old" melting model in Jung, Zhang, and Xue (2008), and (b) the new melting model in this study.

species is again calculated from Equation 5, and finally the corresponding polarimetric radar variables are obtained according to the fitting coefficients in the parameterized forward operators.

2.5. Experimental Design

The parameterized polarimetric radar forward operators depend on water content ($W_x = \rho_a q_x$), characteristic particle mass/volume-weighted mean diameter (D_m) and the percentage of melting (f_{mx}) only. Once the W_x, D_m, and f_{mx} of the melting species are determined from the q and N_t estimates using the aforementioned melting models based on the single-phase hydrometeors from the numerical model, the corresponding radar variables can be calculated using the parameterized forward operators with the same parameterization coefficients as those provided in Section 2.4.1. The melting model is a pre-processing step in the radar forward operators.

In this study, two distinct implementations of parameterized polarimetric radar forward operators are applied, focusing on the simulation of polarimetric radar variables for the real MCS case. Both implementations employ the Zhang et al. (2021) parameterized polarimetric radar forward operators described in Section 2.4.1. However, the original implementation, PFO_Old, utilizes the "old" melting model of Jung, Zhang, and Xue (2008) described in Section 2.4.2, while the updated implementation, PFO_New, utilizes the new melting model described in Section 2.4.3. The simulation and comparison of the polarimetric radar variables are performed on the model grid. By 0100 UTC, the convective system has reached a mature stage and is moving steadily eastward. Multiple times in the mature stage of the convective system were examined and show similar results (see Supporting Information S1). To show the details of the results more clearly with limited figures, only one representative time in part of the simulation domain is shown in the following section. The region for computing Contoured Frequency by Altitude Diagrams (CFADs) and vertical cross-section lines are chosen in the stratiform region to emphasize the ability of PFO_Old and PFO_New to reproduce melting layer features. The value of the CFAD at the given height and radar variables bin is normalized with respect to the total number of grid points at each height.

3. Results

3.1. Reflectivity Factor (Z_H)

Horizontal and vertical sections of observed and simulated Z_H are presented in Figure 2. By 0200 UTC, the leading convection of the MCS extended from western Illinois to northern Missouri, while its trailing stratiform precipitation covered southeastern Iowa (Figure 2a0). Overall, the simulation aptly reproduces the convective and stratiform characteristics observed in the MCS. However, discrepancies in the intensity and structure of the simulated convective system are evident when compared to observations, and these differences vary among the

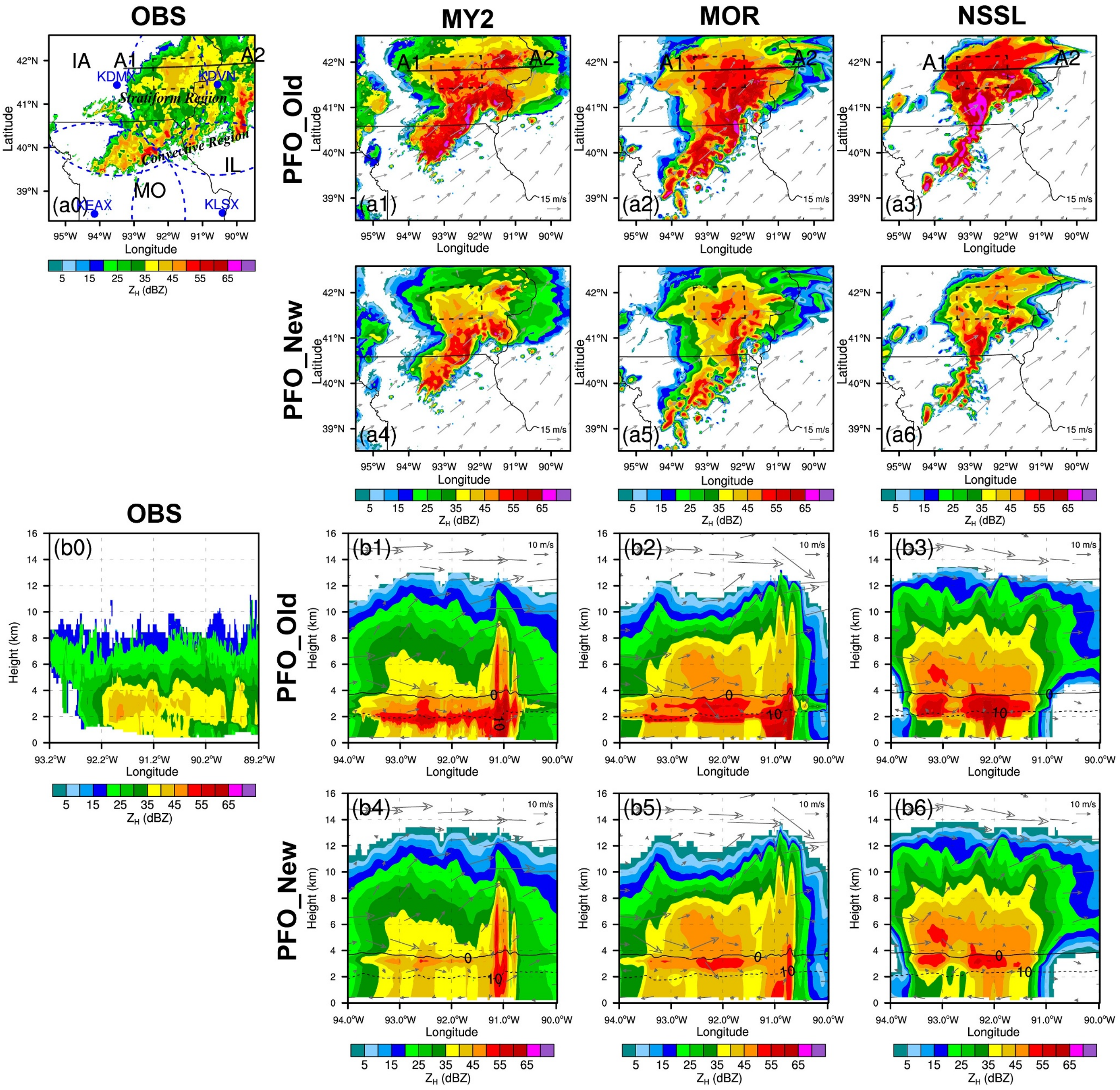

Figure 2. Horizontal cross-section (a0–a6) at $z = 2.5$ km and vertical-section (b0–b6) of observed (a0 and b0) and simulated (a1–a6 and b1–b6) Z_H (dBZ) at 0200 UTC on 29 May 2019. Panels (a1–a3) and (b1–b3) show the PFO_Old for the MY2 (a1 and b1), MOR (a2 and b2) and NSSL (a3 and b3) schemes. Panels (a4–a6) and (b4–b6) show the PFO_New for the MY2 (a4 and b4), MOR (a5 and b5) and NSSL (a6 and b6) schemes. The black solid lines (A1–A2) in (a0–a3) show where vertical cross sections for the observation and each MP scheme are taken. The black dashed rectangular box in (a0–a6) denotes the domain that is used to compute contoured frequency by altitude diagram (CFAD) in the later section. The IA, MO, and IL labels in (a0) are Iowa, Missouri, and Illinois, respectively. The location and maximum range of the radars that primarily provide radar observation are indicated by the blue dots and blue dashed lines in (a0). Note the locations of the stratiform region and convective region. The 0°C (solid line) and 10°C (dash line) isotherms simulated from each MP scheme are shown in (b1–b6).

MP schemes. Notably, PFO_Old exhibits a notable positive bias in simulated Z_H within the stratiform region, with widespread values surpassing 50 dBZ (Figures 2a1–2a3 and 2b1–2b3) at 2.5 km AGL. This positive bias was similarly observed when using the T-Matrix-based forward operator developed by Jung et al. (2010), as reported by Putnam et al. (2017). It is important to note that, in the stratiform precipitation areas, the simulated melting layer signature using PFO_Old across all three MP schemes lie significantly below the 0°C isotherm located at approximately 3.9 km (Figures 2b1–2b3), with maximum Z_H values exceeding 55 dBZ situated at nearly the 10°C isotherm (around 2.1 km). This phenomenon of a melting layer signature that is too low aligns with the same issue noted in the T-Matrix-calculated operator of Jung, Zhang, and Xue (2008) and Jung et al. (2010). Jung et al. attributed this occurrence to the MP scheme's behavior, wherein the melting process occurs at an excessively high ambient temperature. It is noteworthy that this issue persists across the three DM MP schemes employed in this study but is absent in the results diagnosed by the Z_H fields produced by the MP schemes themselves (not shown). This suggests that the issue is not caused by the melting process in the MP schemes but rather by a flaw in the melting model used in the radar forward operator.

Notably, the Z_H simulated by PFO_New (Figures 2a4–2a6 and 2b4–2b6) exhibits better alignment with observations (Figures 2a0 and 2b0) compared to PFO_Old which tends to produce overly high Z_H values. The reduction in Z_H attained through PFO_New is particularly noticeable in the stratiform areas. Additionally, PFO_New maintains the Z_H intensity in convective regions. The melting layer bright band simulated by PFO_New is located immediately below the 0°C isotherm (at about 3.5 km) in all three MP schemes, which is a more reasonable result (Figures 2b4–2b6). Comparing the results of PFO_Old and PFO_New, it is suggested that the "old" melting model and its implementation in the polarimetric radar forward operators may overestimate the contribution of melting ice particles to Z_H. The parameterized forward operators incorporating the new melting model have effectively improved the simulation of melting-layer Z_H in terms of its position and magnitude.

The CFADs of the simulated polarimetric radar variables are constructed for the region indicated by the black box in Figure 2. This region was chosen due to the presence of a distinct melting layer and clear separation from the convective region of the MCS, making it easier to differentiate between the two melting-layer model approaches. CFADs provide a comprehensive view of the distribution of radar variables at different altitudes. In the observed CFAD (Figure 3a0), the melting layer is centered at around 3.0 km AGL, characterized by Z_H values between 40 and 45 dBZ, with some peaks exceeding 50 dBZ. Below the melting layer, Z_H is dominated by rain, with values ranging between 33 and 40 dBZ. PFO_Old simulates a pronounced zone of high Z_H values near the 10°C isotherm in all three MP schemes. This melting layer zone is over 1.5 km thick and features maximum Z_H values at or above 60 dBZ (Figures 3a1–3a3). There is a discontinuity seen in the PFO_Old-simulated Z_H below the 10°C isotherm. This is because PFO_Old diagnoses an erroneously large D_m of melting snow/graupel particles, resulting in pronounced higher Z_H values for these particles at the base of the melting layer compared to the reflectivity of the raindrops immediately beneath them.

In comparison with the results from PFO_Old, the simulations with PFO_New lead to notable improvements in the distributions of Z_H (Figures 3a4–3a6). Across all MP schemes, PFO_New corrects the anomalously high values near the 10°C isotherm observed in the PFO_Old simulations, resulting in a more coherent Z_H distribution from the melting layer to the ground. The comparison of CFADs of the observations and both sets of simulations clearly demonstrates that the incorporation of the new melting model with estimated mixing ratios and number concentrations of melting ice particles into the parameterized forward operators significantly improves the accuracy of the simulated Z_H within the melting layer for all three DM MP schemes examined.

3.2. Differential Reflectivity (Z_{DR})

Z_{DR} is sensitive to the shape, density, phase, and orientation of hydrometeor particles. The observed Z_{DR} pattern in the rain region below the melting layer exhibits a high-value region, exceeding 2.0 dB, in the convective precipitation in northern Missouri, while values are lower, below 2.0 dB, in the stratiform precipitation in eastern Iowa (Figure 4a0). PFO_Old manages to replicate this distribution, with the highest Z_{DR} values in convection regions and lower values in stratiform regions in all three MP schemes. However, their simulated Z_{DR} values in both areas exceed those observed (illustrated in Figures 4a1–4a3). This trend aligns with findings reported in Putnam et al. (2017), where the T-matrix-calculated operator of Jung, Zhang, and Xue (2008) and Jung et al. (2010) similarly yielded higher Z_{DR} values than observed, particularly in stratiform regions. The elevated Z_{DR} regions are primarily situated below the 0°C isotherm, with weak Z_{DR} column signatures appearing in convective regions, around 91.0°W, within the MY2 and MOR schemes (Figures 4b1 and 4b2). Notably, all three MP schemes exhibit an anomalous low-value gap in Z_{DR} around the 10°C isotherm when using PFO_Old, coincident with the highest simulated reflectivity (Figures 2b1–2b3). Examining the simulated Z_{DR} versus D_m for ice particles at a given melting percentage, it was found that Z_{DR} decreases with increasing D_m when ice particles approach complete melting (with a melting percentage exceeding 0.95). This low-value Z_{DR} gap in PFO_Old is

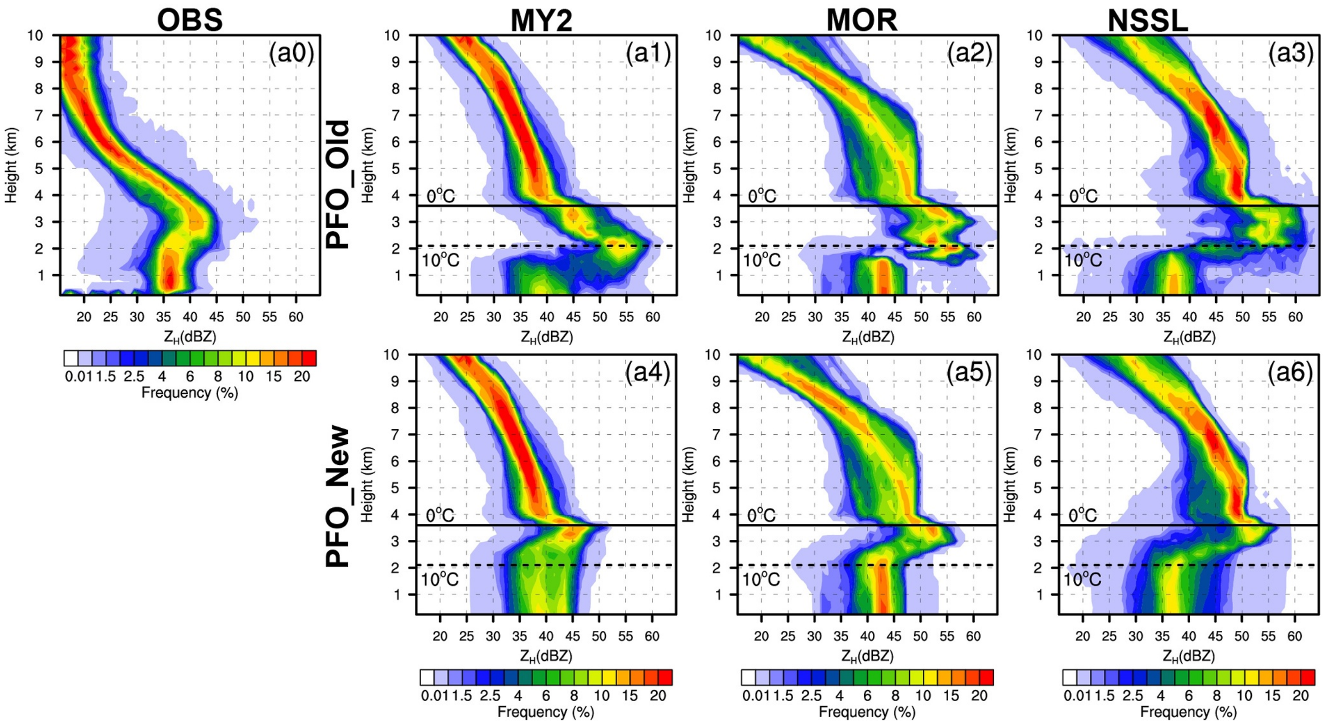

Figure 3. The contoured frequency by altitude diagrams (%) of Z_H (dBZ) using observations (a0) and simulations (a1–a6) from PFO_Old (a1–a3) and PFO_New (a4–a6) within the black dashed rectangular box in Figure 2 at 0200 UTC on 29 May 2019. Panels (a1, a4), (a2, a5), and (a3, a6) show the MY2, MOR, and NSSL schemes, respectively. The 0°C (solid line) and 10°C (dash line) isotherms simulated from each MP scheme are shown in each plot.

caused by oversized near-completely melted ice particles. The concurrent high Z_H and low Z_{DR} values suggest the presence of larger wet snow/graupel particles within this gap.

Comparing PFO_New with PFO_Old, it is evident that the former results in lower Z_{DR} values in both stratiform and convective regions (Figures 4a4–4a6). Specifically, Z_{DR} simulated by PFO_New ranges between 2.2 and 3.4 dB in convective regions across all MP schemes and remains below 2.2 dB in stratiform regions for the MOR and NSSL schemes. Within stratiform regions, the MY2 scheme exhibits the highest Z_{DR}, exceeding 2.2 dB. The vertical cross-section of Z_{DR} shows that PFO_New establishes a more continuous zone of Z_{DR} values at the bottom part of the melting layer (Figures 4b4–4b6). Importantly, the anomalous low-value Z_{DR} gap caused by larger D_m of wet snow/graupel particles in the PFO_Old simulation is successfully eliminated in the PFO_New simulation.

The CFAD of observed Z_{DR} exhibits an area of high values (exceeding 1.6 dB) at the bottom of the melting layer (around 2.5 km height), with Z_{DR} values ranging from 0.8 to 1.6 dB below the melting layer (Figure 5a0). However, the PFO_Old simulation produces unrealistic high Z_{DR} values (over 3.2 dB) at and just below the 10°C isotherm due to the improper treatment of melting snow/graupel particles (Figures 5a1–5a3). PFO_New effectively addresses the issue of unrealistically high Z_{DR} values below the 10°C isotherm (around 2.1 km) and the unphysical Z_{DR} minima at the base of the melting layer observed in the PFO_Old results (Figures 5a4–5a6) in all MP schemes. However, simulated Z_{DR} values are much higher than the observations near the ground for all MP schemes and both PFO_Old and PFO_New. An overestimation of the simulated Z_{DR} below the melting layer can also be found in simulations using the COSMO model (Trömel et al., 2021; Wolfensberger & Berne, 2018). The simulation of the polarimetric signatures of rain is known with a relatively high degree of confidence since the shape, orientations, dielectric constant, etc. of rain are well known. This obvious bias of Z_{DR} in rain would not be caused by the forward operator. It is possible that a systematic model bias exists owing to particles entering the melting layer that may be too rimed and/or too large/aggregated.

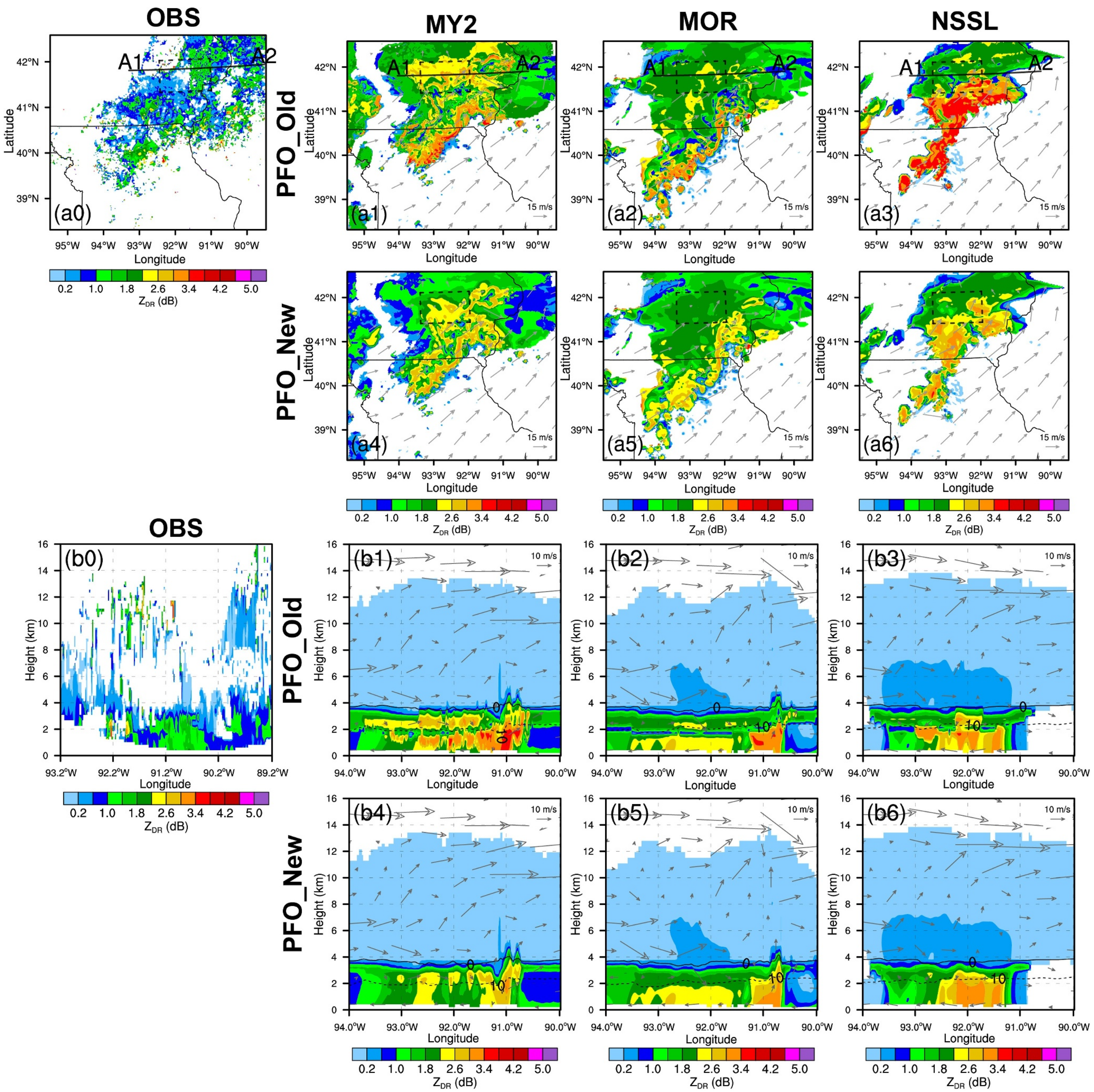

Figure 4. As in Figure 2, but for observed (a0 and b0) and simulated (a1–a6 and b1–b6) Z_{DR} (dB) at 0200 UTC on 29 May 2019. Panels (a1–a3) and (b1–b3) show the PFO_Old for the MY2 (a1 and b1), MOR (a2 and b2), and NSSL (a3 and b3) schemes. Panels (a4–a6) and (b4–b6) show the PFO_New for the MY2 (a4 and b4), MOR (a5 and b5), and NSSL (a6 and b6) schemes.

3.3. Specific Differential Phase (K_{DP})

K_{DP} exhibits strong sensitivity to the concentration of hydrometeor particles. Notably, high K_{DP} values, exceeding 1.0° km^{-1}, are observed in convective regions of northern Missouri, while smaller values are observed in stratiform areas (Figure 6a0). K_{DP} values simulated by PFO_Old mirror these patterns, with an area of high K_{DP} values in convective regions and low K_{DP} values in stratiform areas. As K_{DP} is strongly linked to rainwater content, PFO_New yields similar outcomes to those of PFO_Old (Figures 6a1–6a3 vs. Figures 6a4–6a6). When examining the vertical structure of K_{DP}, a K_{DP} column with values of 0.5 to 1.5° km^{-1} is evident in convective

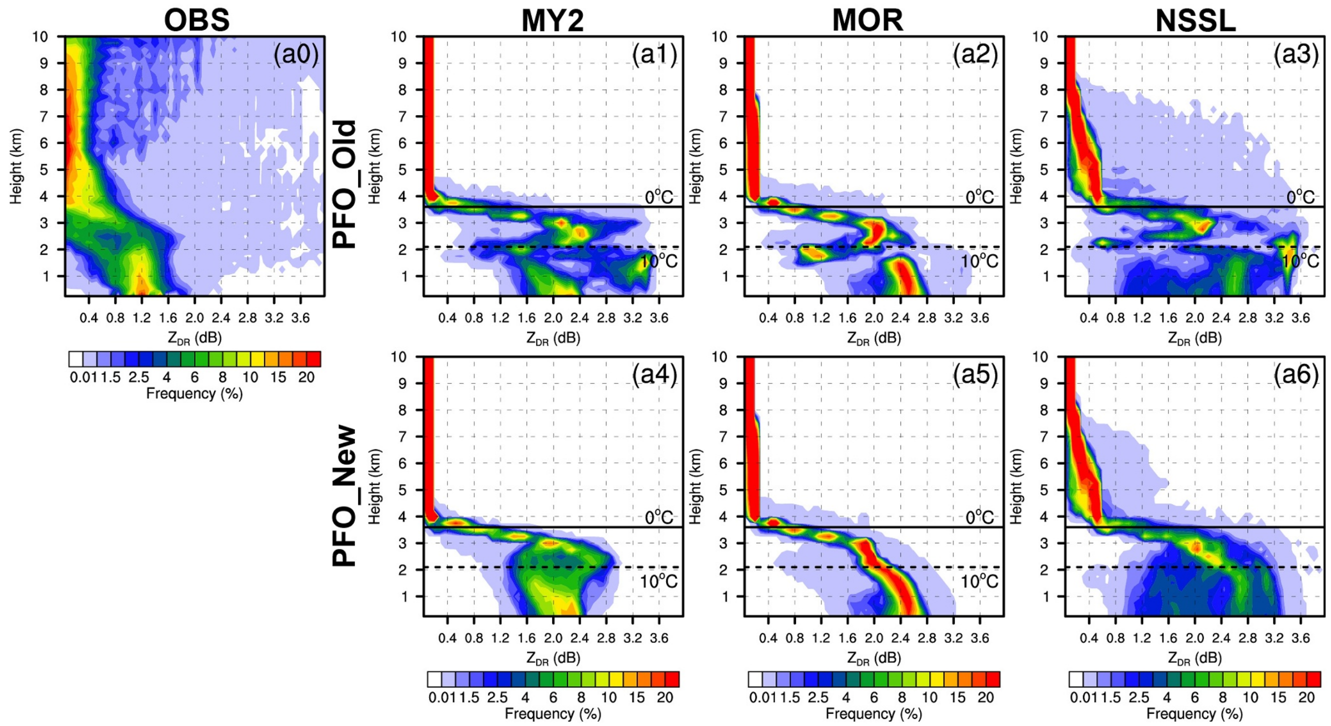

Figure 5. As in Figure 3, but for observations (a0) and simulation (a1–a6) of Z_{DR} (dB) at 0200 UTC on 29 May 2019. (a1–a3) shows the PFO_Old from the MY2 (a1), MOR (a2), and NSSL (a3) schemes. (a4–a6) shows the PFO_New from the MY2 (a4), MOR (a5), and NSSL (a6) schemes.

areas with the MY2 and MOR schemes (Figures 6b1, 6b2, 6b4, and 6b5). Additionally, all three MP schemes reveal a layer with high K_{DP} values situated below the 0°C isotherm, as illustrated in Figures 6b1–6b6.

The CFADs of observed K_{DP} generally remain below $0.4°\ \text{km}^{-1}$, with an area of high K_{DP} (above $0.8°\ \text{km}^{-1}$) at around 3.0 km AGL, corresponding to the area of high reflectivity (Figure 7a0). The K_{DP} distributions simulated by PFO_Old and PFO_New resemble the observed pattern for all MP schemes (Figures 7a1–7a6). However, the simulated K_{DP} appears to have too many medium to high values ($K_{DP} > 0.3°\ \text{km}^{-1}$), particularly in the MY2 and MOR schemes.

3.4. Cross-Correlation Coefficient (ρ_{hv})

The ρ_{hv} provides information regarding the consistency of the shapes and size of particles. Areas with reduced ρ_{hv} values are observed to the east and south of the stratiform region (Figure 8a0). It is noteworthy that the observed ρ_{hv} spans a range from 0.85 to 0.99, whereas simulated ρ_{hv} values have a narrower range from 0.92 to 0.99 (Figures 8a1–a6). It should be noted that T-matrix calculations using spheroids will inherently overestimate ρ_{hv} compared to the observations due to the simplified treatment of hydrometeors. The vertical structure of ρ_{hv}, as simulated by PFO_Old, deviates from the observations, with the bright band occurring close to the 10°C isotherm and lower ρ_{hv} values appearing beneath the bright band (Figures 8b1–8b3). The PFO_New (Figures 8b4–8b6) defines a higher and thinner melting layer compared to PFO_Old. However, the magnitude of ρ_{hv} simulated by PFO_Old fits the observations better than PFO_New. Notably, the radar-observed melting layer is generally a few hundred meters thick (Fabry & Zawadzki, 1995), and even considering the coarser resolution of the model and the effects of interpolation, the melting layer simulated by PFO_Old is too thick and at too low an altitude to be reasonable.

The observed ρ_{hv} CFAD displays a region of low values (around 0.93) at 3.0 km AGL (Figure 9a0). This low-value region of ρ_{hv} also exists in the PFO_Old simulations across all MP schemes, but with a zone near 2.0 km AGL with values near 0.92 (Figures 9a1–9a3). The area of low ρ_{hv} values simulated by PFO_New in the MY2 and MOR schemes (Figures 9a4 and 9a5) is situated around 3.0 km AGL, which aligns well with observations.

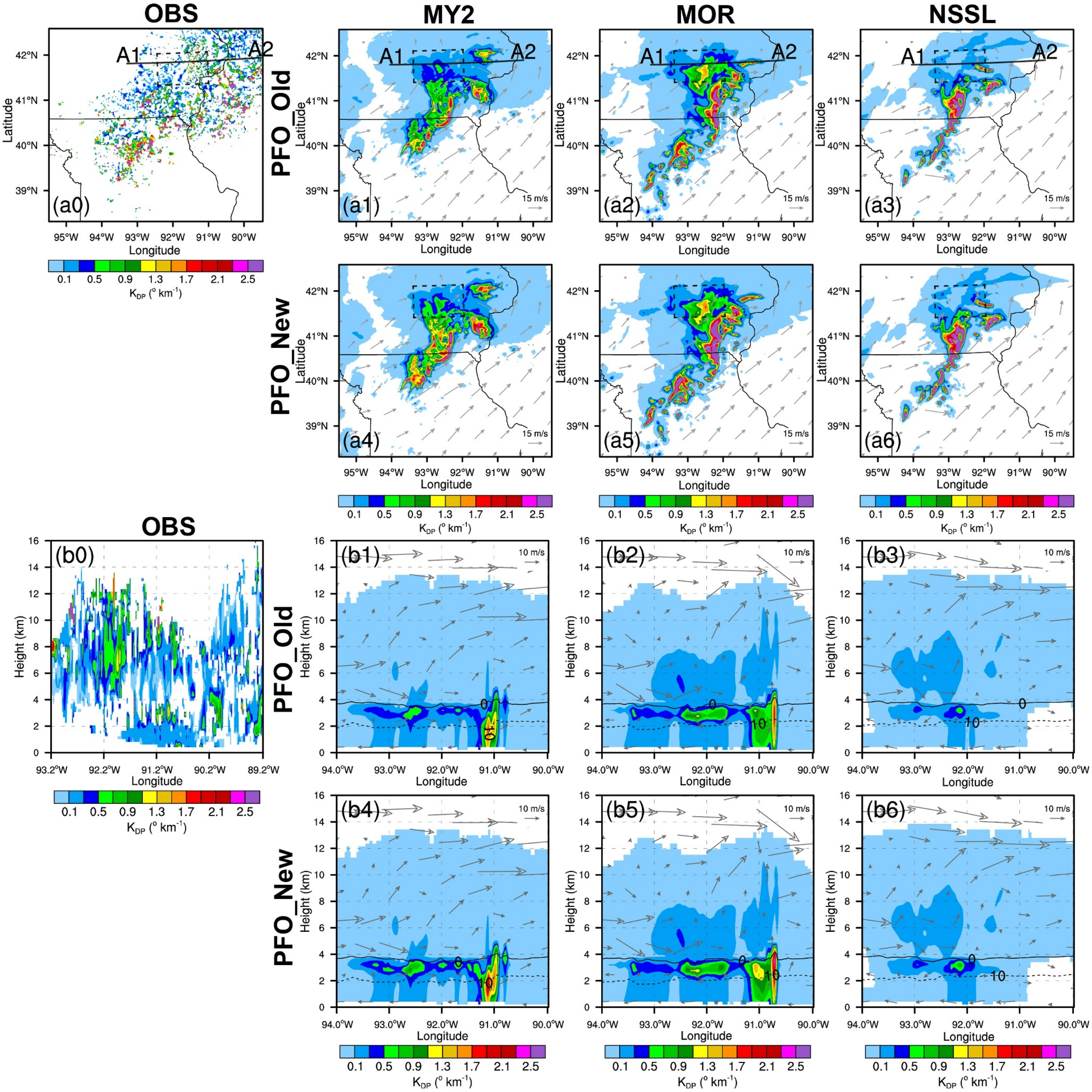

Figure 6. As in Figure 2, but for observed (a0 and b0) and simulated (a1–a6 and b1–b6) K_{DP} (° km^{-1}) at 0200 UTC on 29 May 2019. Panels (a1–a3) and (b1–b3) show the PFO_Old for the MY2 (a1 and b1), MOR (a2 and b2) and NSSL (a3 and b3) schemes. Panels (a4–a6) and (b4–b6) show the PFO_New for the MY2 (a4 and b4), MOR (a5 and b5) and NSSL (a6 and b6) schemes.

3.5. Comparison of the "Old" and New Melting Models

In the parametrized forward operators, simulated polarimetric radar variables are directly related to the D_{m}, water content and the percentage of melting of particles, while the D_{m} is derived from q and N_t. This section reveals the reasons for the improvements when using the new melting model by comparing the q and N_t of melting species estimated by both melting models, as well as the D_{m} of the melting species.

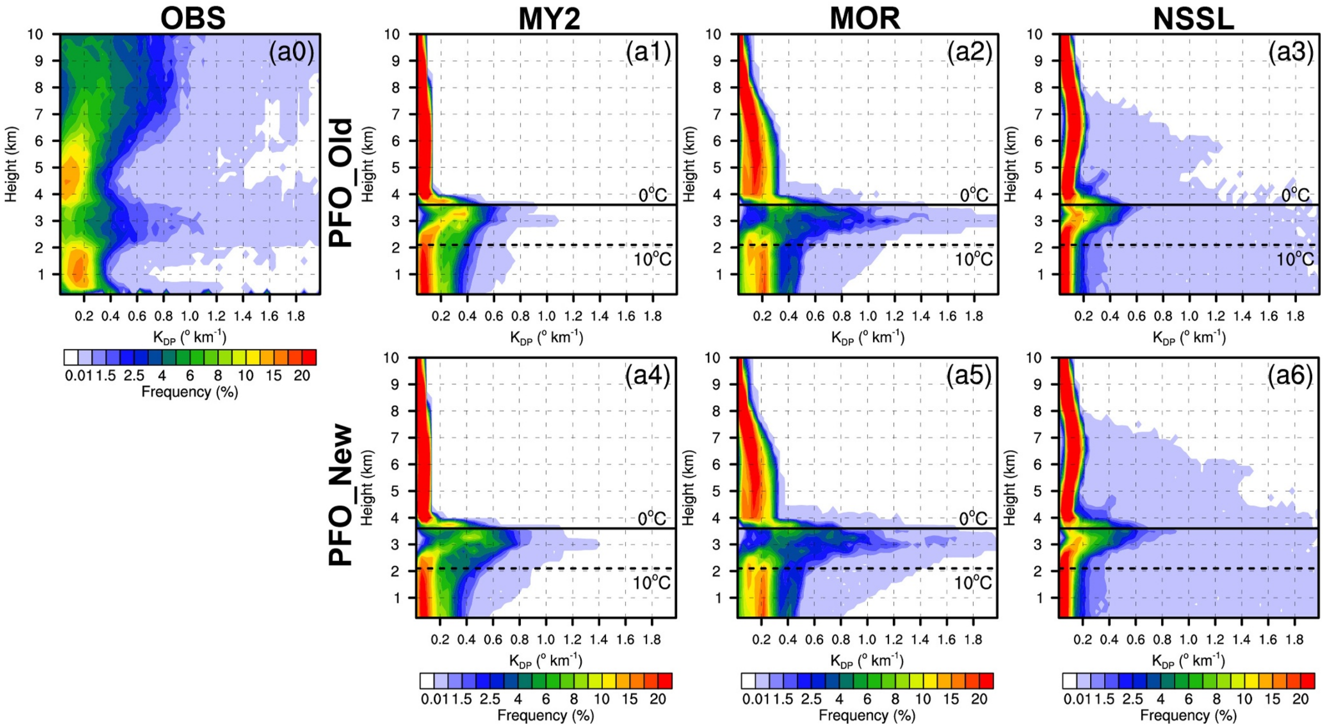

Figure 7. As in Figure 3, but for observations (a0) and simulation (a1–a6) of K_{DP} (° km^{-1}) at 0200 UTC on 29 May 2019. Panels (a1–a3) shows the PFO_Old from the MY2 (a1), MOR (a2), and NSSL (a3) schemes. Panels (a4–a6) shows the PFO_New from the MY2 (a4), MOR (a5), and NSSL (a6) schemes.

3.5.1. Estimating the q and N_t of Melting Species

It is important to emphasize that, as described in Section 2.3, operational DM MP schemes only predict the q and N_t of dry ice particles. Nevertheless, the coexistence of water with ice particles yields distinctive polarimetric signatures, and these interactions are simulated by the polarimetric radar operator, especially in the melting layer. Vertical cross-sections of the mixing ratios of melting ice particles, as simulated by the "old" and new melting models, are presented in Figure 10. Overall, the mixing ratios of melting ice particles estimated by the new melting model (i.e., Equation 15) are similar to those estimated by the "old" melting model (i.e., Equation 12). The mixture of melting ice particles gradually intensifies from the 0°C level down to lower levels, attaining its peak concentration at the 5°C level (approximately 3.0 km in altitude) before decreasing. In the convective region, mixtures of rain and ice are evident above the 0°C level due to strong updrafts. Overall, the "old" and new melting models are capable of generating reasonable distributions of melting ice particles in all three MP schemes, while larger mixing ratios of melting graupel and hail are estimated by the new melting model within strong convection.

The estimated D_{m} used in the parameterized forward operators is jointly determined by N_t and q (i.e., Equation 5). As a result, the polarimetric radar operator requires not only an accurate estimation of the mass content of melting ice particles but also an accurate assessment of their N_t. Figure 11 displays the assumed N_t of melting ice particles in the "old" melting model (i.e., the corresponding N_t of dry ice particles), and the estimated N_t of melting ice particles derived from both dry ice particles and rain in the new melting model. The N_t of dry ice particles rapidly decreases across all MP schemes after passing through the 0°C layer (Figures 11a1–11a3, 11b1, 11 b2, and 11c1–11c3). In the "old" melting model, the very small N_t of dry ice particles at the bottom of the melting layer was incorrectly used as the N_t of melting ice particles and likely contributed to the too-high Z_{H} at the bottom of the melting layer. The N_t of melting ice particles estimated by the new melting model decreases more slowly than those in the "old" melting model after passing through the 0°C layer and reaches zero when the ice species completely melts (Figures 11a4–11a6, 11b4, 11b5, and 11c4–11c6). This approach avoids the use of exceedingly small N_t with moderate mixing ratios near the lower end of the melting layer in the old melting model.

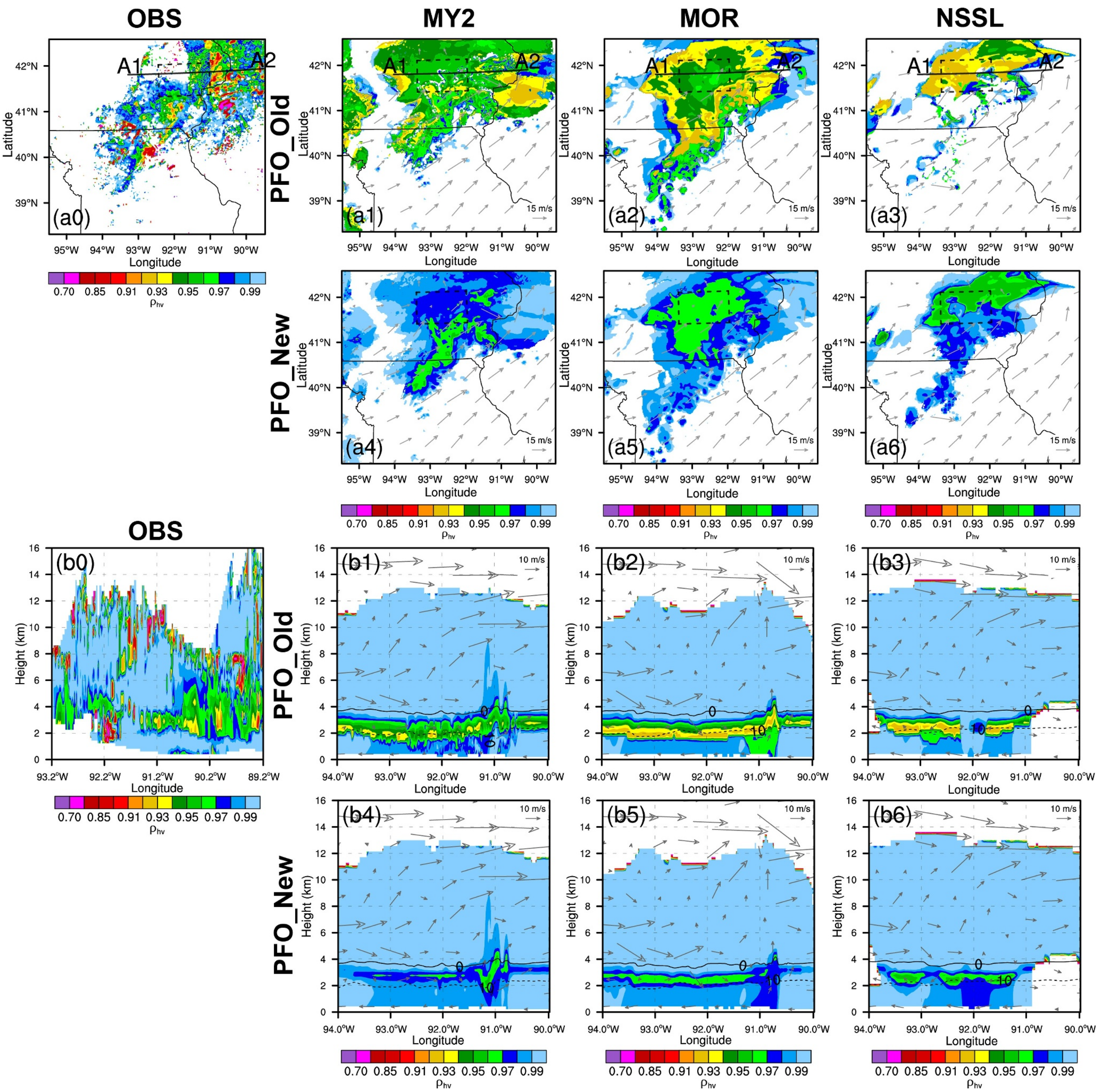

Figure 8. As in Figure 2, but for observed (a0 and b0) and simulated (a1–a6 and b1–b6) ρ_{hv} at 0200 UTC on 29 May 2019. Panels (a1–a3) and (b1–b3) show the PFO_Old for the MY2 (a1 and b1), MOR (a2 and b2) and NSSL (a3 and b3) schemes. Panels (a4–a6) and (b4–b6) show the PFO_New for the MY2 (a4 and b4), MOR (a5 and b5) and NSSL (a6 and b6) schemes.

3.5.2. Estimating the D_m of Melting Species

Figure 12 displays the D_m of rain and melting ice particles from PFO_Old and PFO_New for all MP schemes. With the adjustment of the N_t of melting species by the new melting model, the very high D_m of melting ice particles at the melting layer bottom in the PFO_Old disappears in PFO_New. It is worth noting that the largest D_m of melting ice particles simulated by PFO_Old are not generated at the center of the melting layer but rather emerge at the bottom of the layer, exhibiting unrealistically large diameters—exceeding 10 mm at 2.0-km altitude. The low N_t of dry ice particles at the bottom of the melting layer causes PFO_Old to generate unreasonably large particles. These unreasonably large particles at the lower part of the melting layer result in high Z_H

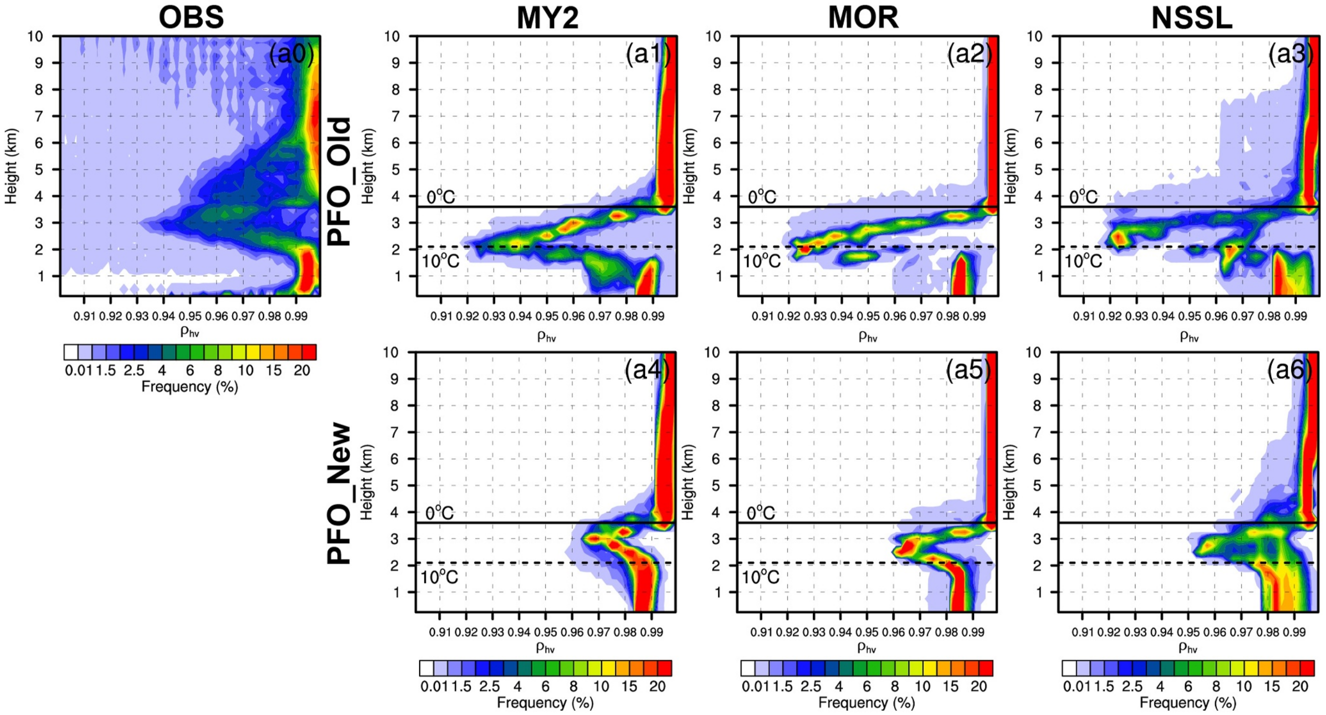

Figure 9. As in Figure 3, but for observations (a0) and simulation (a1–a6) of ρ_{hv} at 0200 UTC on 29 May 2019. Panels (a1–a3) shows the PFO_Old from the MY2 (a1), MOR (a2), and NSSL (a3) schemes. Panels (a4–a6) shows the PFO_New from the MY2 (a4), MOR (a5), and NSSL (a6) schemes.

values, an anomalous Z_{DR} values, and low ρ_{hv} values. Compared to the PFO_Old, the largest D_{m} of melting snow particles—across the three MP schemes—are generated by the PFO_New below the 0°C level at an altitude of 3.0 km in the stratiform region. This makes sense physically, as the D_{m} of the melting species should initially increase as the smallest particles quickly melt, increasing the median particles diameter, followed by a further rapid decrease as even the largest particles melt and shrink. In particular, the adjustment of the number concentrations of melting ice particles in the PFO_New eliminates the very large D_{m} at the melting layer bottom in the PFO_Old.

As previously described, both PFO_Old and PFO_New produce larger Z_{DR} (over 2 dB) than observed near the ground (below 1.0 km altitude), as presented in Figures 5a1–5a6, in regions of predominantly rain. As illustrated in Figures 12a0–12c0, the simulated raindrops have a D_{m} of more than 2 mm near the ground. The simulated Z_{DR} values of over 2 dB are consistent with rain D_{m} exceeding 2 mm (Mahale et al., 2019; Zhang, 2016). This suggests that the overestimation of Z_{DR} is not due to the polarimetric radar operator, but rather to a bias in the MP schemes. All MP schemes simulated a low N_t of raindrops below 10^3 m^{-3} (not shown). These values are lower than those typically observed by disdrometers (Zhang, 2016). The use of large collision-coalescence coefficients, the underestimation of breakup, and/or poor closure assumptions for (rain) N_t tendency during melting in the MP schemes are among the possible reasons for the observed bias.

4. Summary and Discussion

This paper proposes a new melting model for estimating the mixing ratio q and number concentration N_t of melting ice particles, and incorporates these estimates into a set of existing parameterized polarimetric radar forward operators developed by Zhang et al. (2021). The impact of the new melting model on the simulation of polarimetric radar variables is evaluated across three DM bulk MP schemes available within the WRF model: MY2, MOR, and NSSL. A real MCS case, simulated using the WRF model, serves as input for two implementations of the parameterized forward operators which simulate Z_{H}, Z_{DR}, K_{DP}, and ρ_{hv}. One implementation (PFO_Old) employs the old melting model of Jung, Zhang, and Xue (2008) in the parameterized forward operators while the other implementation (PFO_New) uses the new melting model.

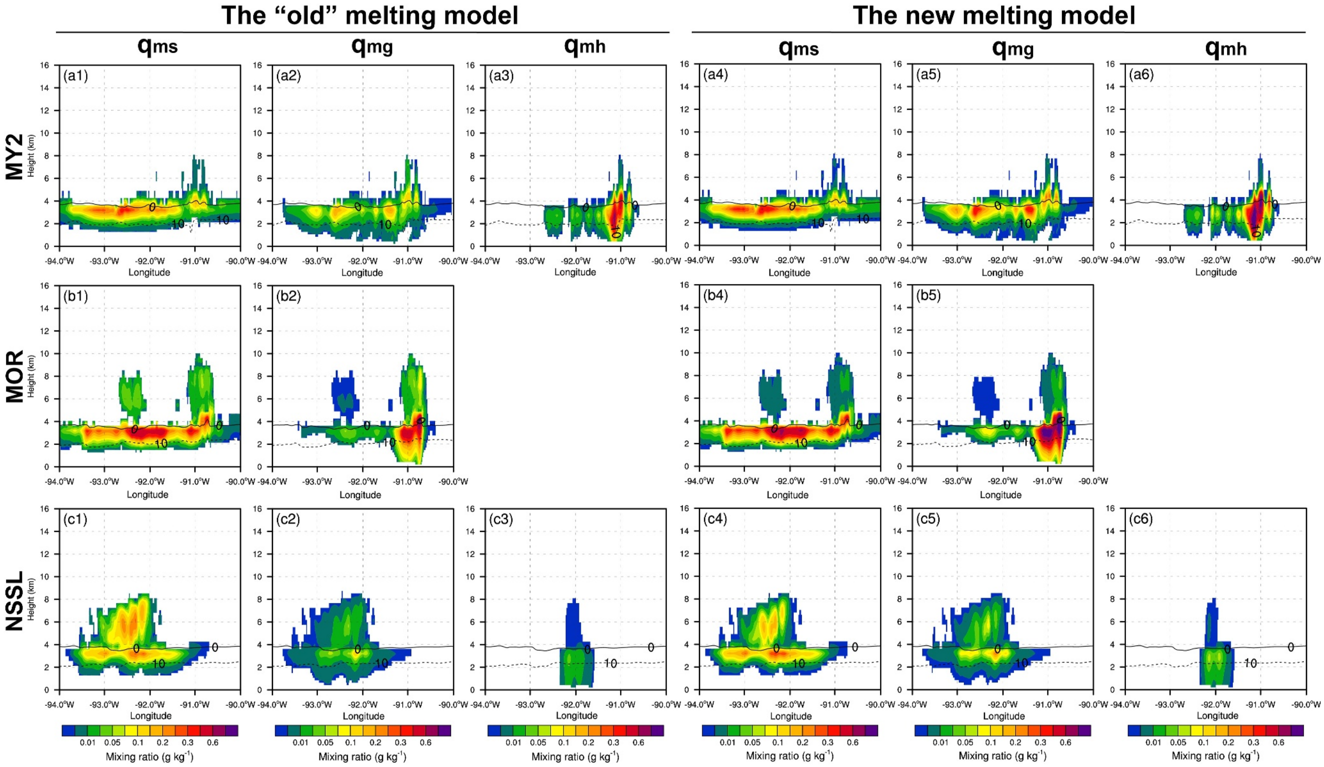

Figure 10. The vertical cross-section of estimated mixing ratios (g kg^{-1}) of melting ice particles from the "old" (a1–a3, b1–b2, and c1–c3) and new (a4–a5, b4–b5, and c4–c6) melting model along with line A1–A2 in Figure 2 at 0200 UTC on 29 May 2019 for (a1–c1 and a4–c4) melting snow, (a2–c2 and a5–c5) melting graupel, and (a3, c3 and a6, c6) melting hail using the (a1–a6) MY2, (b1–b5) MOR, and (c1–c6) NSSL schemes. The 0°C (solid line) and 10°C (dash line) isotherms are shown in each plot.

Across all MP schemes, PFO_Old is capable of reproducing the observed polarimetric signatures of the MCS in a general sense, but there are some unrealistic phenomena, such as higher Z_H and Z_{DR} in stratiform regions, a bright band that is too low and thick, and an anomalous low-value gap of Z_{DR} at the bottom of the melting layer. The PFO_Old-simulated CFADs of Z_H, Z_{DR}, and ρ_{hv} exhibit an unphysical discontinuity below the 10°C isotherm across all three MP schemes. Similar to the PFO_Old, the operators based on the numerically integrated T-matrix-based operator by Jung, Zhang, and Xue (2008) and Jung et al. (2010) also produce excessively high Z_H and Z_{DR} in the stratiform region of MCSs, particularly in the MY2 and MOR schemes (Putnam et al., 2017). The failure of the melting model to reasonably estimate the number concentrations of melting species leads these operators to produce very large D_m at the melting layer bottom. The overestimation of the D_m of melting ice particles leads to the creation of an overly intense, thick, and low-altitude melting layer in the stratiform region than observed.

Compared to PFO_Old, PFO_New utilizing the newly developed melting model eliminates the very large D_m at the melting layer bottom, mitigates the unrealistic melting-layer signatures in PFO_Old, and shows improved simulated polarimetric radar variables for all three DM MP schemes, suggesting that the implicit estimates of mixing ratios and number concentrations of the melting species are more reasonable. This improvement results in a relatively subdued, narrower, and more reasonably located melting layer within the stratiform region. The simulated bright band of the melting layer, as generated by PFO_New, lies beneath the 0°C isotherm (around 3.5 km) across the three MP schemes—representing a more realistic outcome. CFADs of the polarimetric radar variables demonstrate that PFO_New yields smoother transitions into and out of the melting layer than PFO_Old.

The coexistence of water and ice particles plays an integral role in many well-known polarimetric signatures. Within stratiform melting layers, the non-uniform shape of melting snow introduces a scattering effect that leads to notable reductions in ρ_{hv} at common weather radar wavelengths. Meanwhile, in convective updrafts, the presence of a mixture of supercooled drops and water-coated ice particles contributes to Z_{DR} columns, as detailed by Kumjian et al. (2014). Additionally, the K_{DP} column is linked to raindrops shed from hailstones (Hubbert et al., 1998), as well as high concentrations of raindrops and melting graupel more generally (Kumjian &

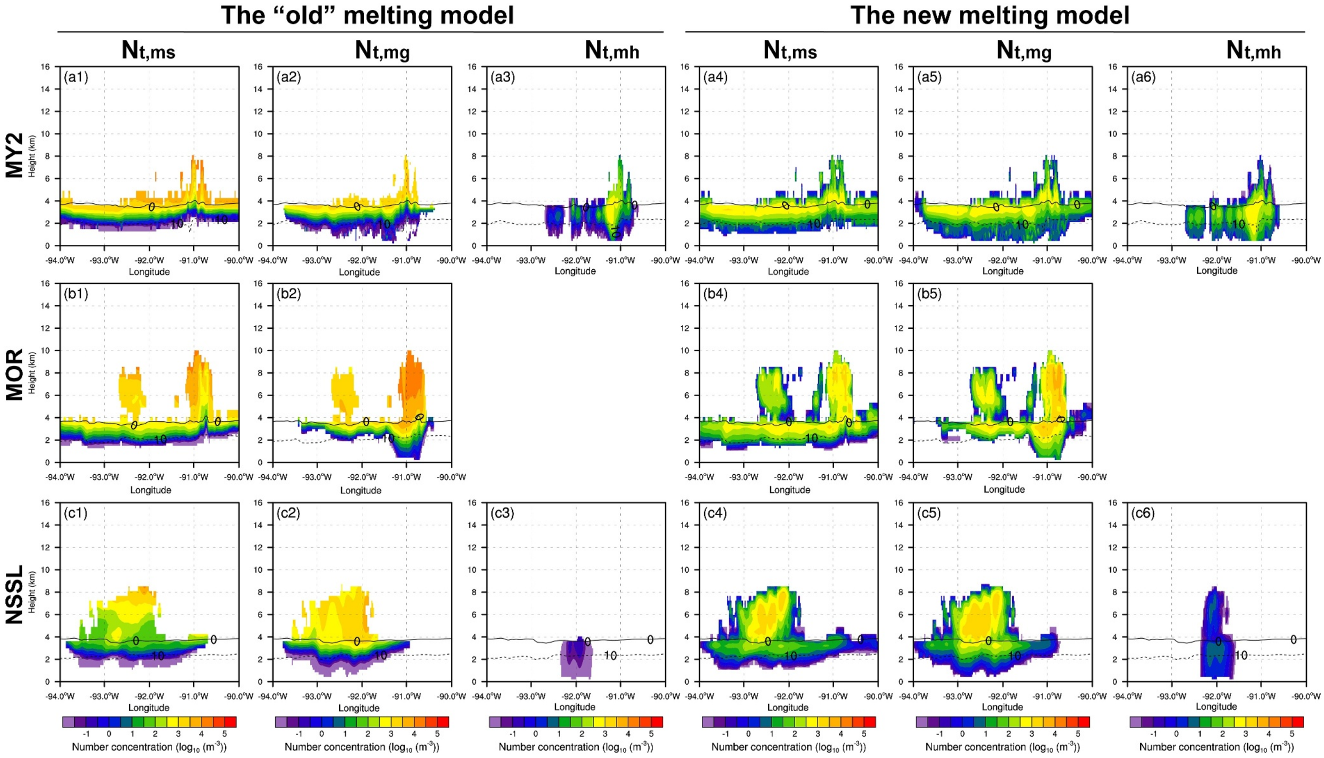

Figure 11. As in Figure 10, but for number concentrations ($\log_{10}(\mathrm{m}^{-3})$) of melting ice. In the "old" melting model, the number concentration of the dry ice particles with mixing ratios of melting ice particles over zero was used as the corresponding number concentration of melting ice particles. Panels (a1–a3), (b1, b2), and (c1–c3) also are the corresponding number concentrations of dry ice particles.

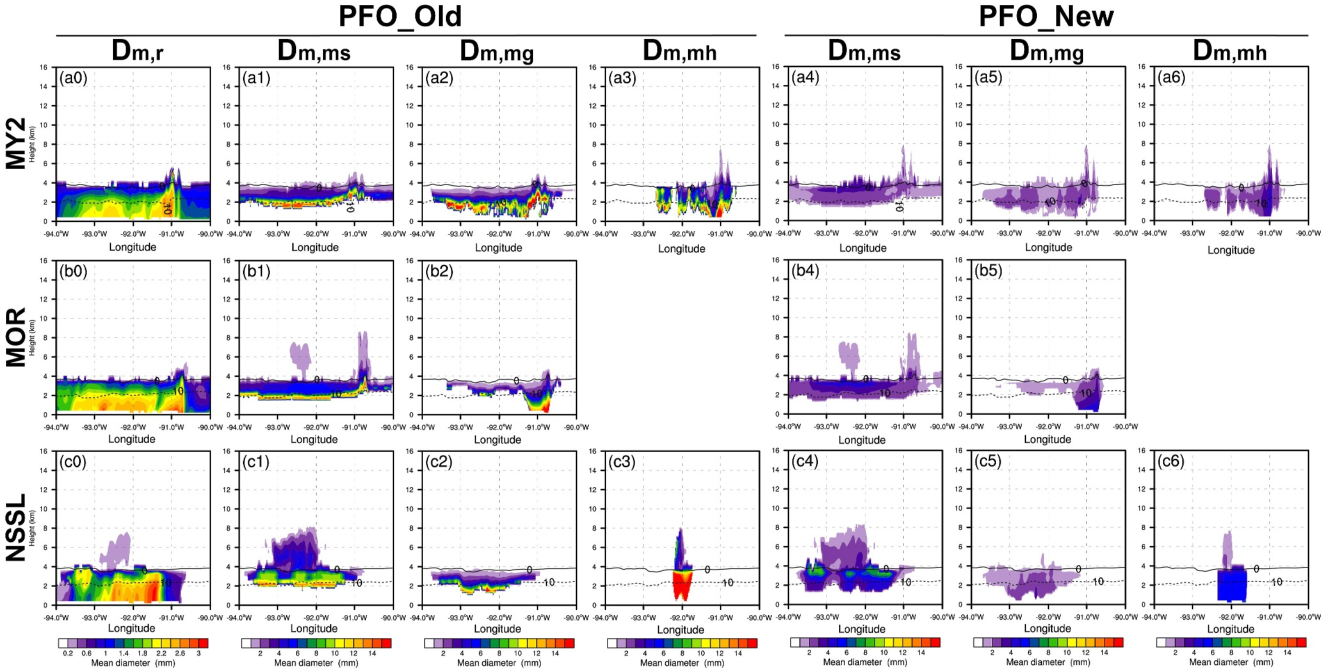

Figure 12. The vertical cross-section of simulated mass/volume-weighted mean diameter (D_m in mm) for rain (a0–c0) from PFO_Old and melting snow (a1–c1 and a4–c4), melting graupel (a2–c2 and a5–c5), and melting hail (a3, c3 and a6, c6) from PFO_Old and PFO_New along with line A1–A1 in Figure 2 at 0200 UTC on 29 May 2019 using the (a0–a6) MY2, (b0–b5) MOR, and (c0–c6) NSSL schemes. The 0°C (solid line) and 10°C (dash line) isotherms are shown in each plot. Notably, the simulated D_m for rain from PFO_Old and PFO_New is nearly the same.

Ryzhkov, 2008). Given that most existing operational DM bulk MP schemes currently consist only of single-phase hydrometeor species such as cloud water, rain, and dry ice particles (e.g., snow, graupel, and hail), the adoption of a melting model within the polarimetric radar forward operator serves as a practical solution for realistically simulating the polarimetric signatures of melting hydrometeors. Some recently developed MP schemes using generalized property-based ice-phase categories (e.g., P3 and ISHMAEL) represent ice-phase hydrometeors and growth/decay processes more realistically than traditional MP schemes that use predefined ice-phase categories (e.g., snow, graupel, and hail) with fixed physical properties. The P3 scheme can predict liquid fraction which enables an explicit representation of mixed-phase particles.

Additionally, across three DM MP schemes, an underestimation of N_t in rain leads to the overestimation of D_m of raindrops in this case. The simulated Z and Z_{DR} values by the polarimetric radar simulator are much higher than typical observations both near the ground and immediately below the melting layer for all MP schemes, suggesting that the particles entering the melting layer may be either too rimed or too large/aggregated in NWP models. It is relevant in the broader context that even a perfect operator will not match observations if there are inherent limitations in the underlying MP schemes. There are seemingly systematic biases in the output of the NWP models that need to be considered when developing operators and comparing simulated and observed variables. Therefore, improving MP schemes by refining the collision-coalescence coefficients, improving the representativeness of breakup processes, and rationalizing closure assumptions for the N_t (rain) tendency during melting in the MP schemes may result in more realistic simulated polarimetric features and improve the numerical model itself by simulating cloud microphysics processes more accurately.

Data Availability Statement

For this work, the NEXRAD Level-II data used in this research can be accessed at the National Oceanic and Atmospheric Administration (NOAA) National Centers for Environmental Information website (http://www.ncei.noaa.gov) by filling in locations of radar site (KDMX, KEAX, KDVN, KLSX) and date (0200 UTC on 29 May 2019) (NOAA, 2015). More information about the NEXRAD radars can be found at https://www.ncei.noaa.gov/products/radar/next-generation-weather-radar. The WRF source code version 3.7.1 (Skamarock et al., 2008) is publicly available at NCAR/UCAR (https://github.com/wrf-model/WRF).

Acknowledgments
This work was supported by the NSF Grant 2136161. Funding was also provided by NOAA/Office of Oceanic and Atmospheric Research under NOAA-University of Oklahoma Cooperative Agreement NA21OAR4320204, U.S. Department of Commerce. The computing for this project was performed at the OU Supercomputing Center for Education and Research (OSCER) at the University of Oklahoma (OU) and the Anvil CPU at Purdue University through allocation EES220057 from the Advanced Cyberinfrastructure Coordination Ecosystem: Services & Support (ACCESS) program, which is supported by National Science Foundation Grants 2138259, 2138286, 2138307, 2137603, and 2138296. We thank the three anonymous reviewers for their helpful comments on the manuscript.

References

Augros, C., Caumont, O., Ducrocq, V., Gaussiat, N., & Tabary, P. (2016). Comparisons between S-C- and X-band polarimetric radar observations and convective-scale simulations of the HyMeX first special observing period. *Quarterly Journal of the Royal Meteorological Society*, *142*(S1), 347–362. https://doi.org/10.1002/qj.2572

Blahak, U. (2016). RADAR MIE LM and RADAR MIELIB–calculation of radar reflectivity from model output. In *COSMO technical report no. 28. Consortium for small scale modeling*. https://doi.org/10.5676/DWDpub/nwv/cosmo-tr28

Carlin, J. T., Gao, J., Snyder, J. C., & Ryzhkov, A. V. (2017). Assimilation of ZDR columns for improving the spinup and forecast of convective storms in storm-scale models: Proof-of-concept experiments. *Monthly Weather Review*, *145*(12), 5033–5057. https://doi.org/10.1175/mwr-d-17-0103.1

Chen, G., Zhao, K., Huang, H., Yang, Z., Lu, Y., & Yang, J. (2021). Evaluating simulated raindrop size distributions and ice microphysical processes with polarimetric radar observations in a Meiyu front event over eastern China. *Journal of Geophysical Research: Atmospheres*, *126*(22), e2020JD034511. https://doi.org/10.1029/2020JD034511

Cholette, M., Milbrandt, J. A., Morrison, H., Paquin-Ricard, D., & Jacques, D. (2023). Combining triple-moment ice with prognostic liquid fraction in the P3 microphysics scheme: Impacts on a simulated squall line. *Journal of Advances in Modeling Earth Systems*, *15*(4), e2022MS003328. https://doi.org/10.1029/2022MS003328

Dawson, D. T., Mansell, E. R., Jung, Y., Wicker, L. J., Kumjian, M. R., & Xue, M. (2014). Low-level ZDR signatures in supercell forward flanks: The role of size sorting and melting of hail. *Journal of the Atmospheric Sciences*, *71*(1), 276–299. https://doi.org/10.1175/jas-d-13-0118.1

Ding, Z., Zhao, K., Zhu, K., Feng, Y., Huang, H., & Yang, Z. (2022). Assimilation of polarimetric radar observation with GSI cloud analysis for the prediction of a squall line. *Geophysical Research Letters*, *49*(16), e2022GL098253. https://doi.org/10.1029/2022gl098253

Du, M., Gao, J., Zhang, G., Wang, Y., Heiselman, P. L., & Cui, C. (2021). Assimilation of polarimetric radar data in simulation of a supercell storm with a variational approach and the WRF model. *Remote Sensing-Basel*, *13*(16), 3060. https://doi.org/10.3390/rs13163060

Fabry, F., & Zawadzki, I. (1995). Long-term radar observations of the melting layer of precipitation and their interpretation. *Journal of the Atmospheric Sciences*, *52*(7), 838–851. https://doi.org/10.1175/1520-0469(1995)052<0838:LTROOT>2.0.CO;2

Girard, C., Plante, A., Desgagné, M., McTaggart-Cowan, R., Côté, J., Charron, M., et al. (2014). Staggered vertical discretization of the Canadian Environmental Multiscale (GEM) model using a coordinate of the log-hydrostatic-pressure type. *Monthly Weather Review*, *142*(3), 1183–1196. https://doi.org/10.1175/MWR-D-13-00255.1

Hong, S.-Y., Noh, Y., & Dudhia, J. (2006). A new vertical diffusion package with an explicit treatment of entrainment processes. *Monthly Weather Review*, *134*(9), 2318–2341. https://doi.org/10.1175/MWR3199.1

Hubbert, J., Bringi, V. N., Carey, L. D., & Bolen, S. (1998). CSU-CHILL polarimetric radar measurements from a severe hail storm in eastern Colorado. *Journal of Applied Meteorology*, *37*(8), 749–775. https://doi.org/10.1175/1520-0450(1998)037<0749:CCPRMF>2.0.CO;2

Iacono, M. J., Delamere, J. S., Mlawer, E. J., Shephard, M. W., Clough, S. A., & Collins, W. D. (2008). Radiative forcing by long-lived greenhouse gases: Calculations with the AER radiative transfer models. *Journal of Geophysical Research*, *113*(D13), D13103. https://doi.org/10.1029/2008JD009944

Jensen, A. A., Harrington, J. Y., Morrison, H., & Milbrandt, J. A. (2017). Predicting ice shape evolution in a bulk microphysics model. *Journal of the Atmospheric Sciences*, *74*(6), 2081–2104. https://doi.org/10.1175/JAS-D-16-0350.1

Johnson, M., Jung, Y., Dawson, D. T., & Xue, M. (2016). Comparison of simulated polarimetric signatures in idealized supercell storms using two-moment bulk microphysics schemes in WRF. *Monthly Weather Review*, *144*(3), 971–996. https://doi.org/10.1175/mwr-d-15-0233.1

Jung, Y., Xue, M., & Tong, M. (2012). Ensemble Kalman filter analyses of the 29–30 May 2004 Oklahoma tornadic thunderstorm using one- and two-moment bulk microphysics schemes, with verification against polarimetric radar data. *Monthly Weather Review*, *140*(5), 1457–1475. https://doi.org/10.1175/MWR-D-11-00032.1

Jung, Y., Xue, M., & Zhang, G. (2010). Simulations of polarimetric radar signatures of a supercell storm using a two-moment bulk microphysics scheme. *Journal of Applied Meteorology and Climatology*, *49*(1), 146–163. https://doi.org/10.1175/2009jamc2178.1

Jung, Y., Xue, M., Zhang, G., & Straka, J. M. (2008). Assimilation of simulated polarimetric radar data for a convective storm using the ensemble Kalman filter. Part II: Impact of polarimetric data on storm analysis. *Monthly Weather Review*, *136*(6), 2246–2260. https://doi.org/10.1175/2007mwr2288.1

Jung, Y., Zhang, G., & Xue, M. (2008). Assimilation of simulated polarimetric radar data for a convective storm using the ensemble Kalman filter. Part I: Observation operators for reflectivity and polarimetric variables. *Monthly Weather Review*, *136*(6), 2228–2245. https://doi.org/10.1175/2007mwr2083.1

Kumjian, M. R., Khain, A. P., Benmoshe, N., Ilotoviz, E., Ryzhkov, A. V., & Phillips, V. T. J. (2014). The anatomy and physics of ZDR columns: Investigating a polarimetric radar signature with a spectral bin microphysical model. *Journal of Applied Meteorology and Climatology*, *53*(7), 1820–1843. https://doi.org/10.1175/jamc-d-13-0354.1

Kumjian, M. R., & Ryzhkov, A. V. (2008). Polarimetric signatures in supercell thunderstorms. *Journal of Applied Meteorology and Climatology*, *47*(7), 1940–1961. https://doi.org/10.1175/2007jamc1874.1

Kumjian, M. R., Ryzhkov, A. V., Melnikov, V. M., & Schuur, T. J. (2010). Rapid-scan super-resolution observations of a cyclic supercell with a dual-polarization WSR-88D. *Monthly Weather Review*, *138*(10), 3762–3786. https://doi.org/10.1175/2010MWR3322.1

Li, X., Mecikalski, J. R., Otkin, J. A., Henderson, D. S., & Srikishen, J. (2022). A polarimetric radar operator and application for convective storm simulation. *Atmosphere*, *13*(5), 645. https://doi.org/10.3390/atmos13050645

Mahale, V. N., Zhang, G., Xue, M., Gao, J., & Reeves, H. D. (2019). Variational retrieval of rain microphysics and related parameters from polarimetric radar data with a parameterized operator. *Journal of Atmospheric and Oceanic Technology*, *36*(12), 2483–2500. https://doi.org/10.1175/jtech-d-18-0212.1

Mansell, E. R., Ziegler, C. L., & Bruning, E. C. (2010). Simulated electrification of a small thunderstorm with two-moment bulk microphysics. *Journal of the Atmospheric Sciences*, *67*(1), 171–194. https://doi.org/10.1175/2009jas2965.1

Matsui, T., Dolan, B., Rutledge, S. A., Tao, W. K., Iguchi, T., Barnum, J., & Lang, S. E. (2019). POLARRIS: A POLArimetric radar retrieval and instrument simulator. *Journal of Geophysical Research: Atmospheres*, *124*(8), 4634–4657. https://doi.org/10.1029/2018jd028317

Milbrandt, J. A., & Morrison, H. (2013). Prediction of graupel density in a bulk microphysics scheme. *Journal of the Atmospheric Sciences*, *70*(2), 410–429. https://doi.org/10.1175/JAS-D-12-0204.1

Milbrandt, J. A., Morrison, H., DawsonII, D. T., & Paukert, M. (2021). A triple-moment representation of ice in the predicted particle properties (P3) microphysics scheme. *Journal of the Atmospheric Sciences*, *78*(2), 439–458. https://doi.org/10.1175/JAS-D-20-0084.1

Milbrandt, J. A., & Yau, M. (2005a). A multimoment bulk microphysics parameterization. Part I: Analysis of the role of the spectral shape parameter. *Journal of the Atmospheric Sciences*, *62*(9), 3051–3064. https://doi.org/10.1175/jas3534.1

Milbrandt, J. A., & Yau, M. (2005b). A multimoment bulk microphysics parameterization. Part II: A proposed three-moment closure and scheme description. *Journal of the Atmospheric Sciences*, *62*(9), 3065–3081. https://doi.org/10.1175/jas3535.1

Morrison, H., & Milbrandt, J. A. (2015). Parameterization of cloud microphysics based on the prediction of bulk ice particle properties. Part I: Scheme description and idealized tests. *Journal of the Atmospheric Sciences*, *72*(1), 287–311. https://doi.org/10.1175/JAS-D-14-0065.1

Morrison, H., Thompson, G., & Tatarskii, V. (2009). Impact of cloud microphysics on the development of trailing stratiform precipitation in a simulated squall line: Comparison of one-and two-moment schemes. *Monthly Weather Review*, *137*(3), 991–1007. https://doi.org/10.1175/2008mwr2556.1

National Oceanic and Atmospheric Administration (NOAA). (2015). The Next Generation Weather Radar (NEXRAD) level-II data [Dataset]. *National Centers for Environmental Information (NCEI)*. Retrieved from https://www.ncei.noaa.gov

Oue, M., Tatarevic, A., Kollias, P., Wang, D., Yu, K., & Vogelmann, A. M. (2020). The Cloud-resolving model Radar SIMulator (CR-SIM) version 3.3: Description and applications of a virtual observatory. *Geoscientific Model Development*, *13*(4), 1975–1998. https://doi.org/10.5194/gmd-13-1975-2020

Picca, J. C., Schultz, D. M., Colle, B. A., Ganetis, S., Novak, D. R., & Sienkiewicz, M. J. (2014). The value of dual-polarization radar in diagnosing the complex microphysical evolution of an intense snowband. *Bulletin of the American Meteorological Society*, *95*(12), 1825–1834. https://doi.org/10.1175/BAMS-D-13-00258.1

Putnam, B. J., Jung, Y., Yussouf, N., Stratman, D., Supinie, T. A., Xue, M., et al. (2021). The impact of assimilating ZDR observations on storm-scale ensemble forecasts of the 31 May 2013 Oklahoma storm event. *Monthly Weather Review*, *149*(6), 1919–1942. https://doi.org/10.1175/MWR-D-20-0261.1

Putnam, B. J., Xue, M., Jung, Y., Snook, N., & Zhang, G. (2014). The analysis and prediction of microphysical states and polarimetric radar variables in a mesoscale convective system using double-moment microphysics, multinetwork radar data, and the ensemble Kalman filter. *Monthly Weather Review*, *142*(1), 141–162. https://doi.org/10.1175/mwr-d-13-00042.1

Putnam, B. J., Xue, M., Jung, Y., Snook, N., & Zhang, G. (2019). Ensemble Kalman filter assimilation of polarimetric radar observations for the 20 May 2013 Oklahoma tornadic supercell case. *Monthly Weather Review*, *147*(7), 2511–2533. https://doi.org/10.1175/mwr-d-18-0251.1

Putnam, B. J., Xue, M., Jung, Y., Zhang, G., & Kong, F. (2017). Simulation of polarimetric radar variables from 2013 CAPS spring experiment storm-scale ensemble forecasts and evaluation of microphysics schemes. *Monthly Weather Review*, *145*(1), 49–73. https://doi.org/10.1175/mwr-d-15-0415.1

Romine, G. S., Burgess, D. W., & Wilhelmson, R. B. (2008). A dual-polarization-radar-based assessment of the 8 May 2003 Oklahoma City area tornadic supercell. *Monthly Weather Review*, *136*(8), 2849–2870. https://doi.org/10.1175/2008MWR2330.1

Ryzhkov, A., Pinsky, M., Pokrovsky, A., & Khain, A. (2011). Polarimetric radar observation operator for a cloud model with spectral microphysics. *Journal of Applied Meteorology and Climatology*, *50*(4), 873–894. https://doi.org/10.1175/2010jamc2363.1

Shrestha, P., Mendrok, J., & Brunner, D. (2022). Aerosol characteristics and polarimetric signatures for a deep convective storm over the northwestern part of Europe—Modeling and observations. *Atmospheric Chemistry and Physics*, *22*(21), 14095–14117. https://doi.org/10.5194/acp-22-14095-2022

Shrestha, P., Mendrok, J., Pejcic, V., Trömel, S., Blahak, U., & Carlin, J. T. (2022). Evaluation of the COSMO model (v5.1) in polarimetric radar space—Impact of uncertainties in model microphysics, retrievals and forward operators. *Geoscientific Model Development*, *15*(1), 291–313. https://doi.org/10.5194/gmd-15-291-2022

Shrestha, P., Trömel, S., Evaristo, R., & Simmer, C. (2022). Evaluation of modelled summertime convective storms using polarimetric radar observations. *Atmospheric Chemistry and Physics*, *22*(11), 7593–7618. https://doi.org/10.5194/acp-22-7593-2022

Skamarock, W. C., Klemp, J. B., Dudhia, J., Gill, D. O., Barker, D. M., Duda, M. G., et al. (2008). A description of the advanced research WRF version 3 (no. NCAR/TN-475+STR) [Software]. *National Center for Atmospheric Research Boulder*, *475*, 113. https://doi.org/10.5065/D68S4MVH

Snyder, J. C., Bluestein, H. B., DawsonII, D. T., & Jung, Y. (2017a). Simulations of polarimetric, X-band radar signatures in supercells. Part I: Description of experiment and simulated ρhv rings. *Journal of Applied Meteorology and Climatology*, *56*(7), 1977–1999. https://doi.org/10.1175/jamc-d-16-0138.1

Snyder, J. C., Bluestein, H. B., DawsonII, D. T., & Jung, Y. (2017b). Simulations of polarimetric, X-band radar signatures in supercells. Part II: ZDR columns and rings and KDP columns. *Journal of Applied Meteorology and Climatology*, *56*(7), 2001–2026. https://doi.org/10.1175/jamc-d-16-0139.1

SPC. (2019). *SPC filtered storm reports for 5/28/2019*. NOAA/NWS/Storm Prediction Center. Retrieved from https://www.spc.noaa.gov/climo/reports/190528_rpts.html

Stensrud, D. J., Wicker, L. J., Xue, M., Dawson, D. T., Yussouf, N., Wheatley, D. M., et al. (2013). Progress and challenges with warn-on-forecast. *Atmospheric Research*, *123*, 2–16. https://doi.org/10.1016/j.atmosres.2012.04.004

Stensrud, D. J., Xue, M., Wicker, L. J., Kelleher, K. E., Foster, M. P., Schaefer, J. T., et al. (2009). Convective-scale warn-on-forecast system: A vision for 2020. *Bulletin of the American Meteorological Society*, *90*(10), 1487–1500. https://doi.org/10.1175/2009BAMS2795.1

Trömel, S., Simmer, C., Blahak, U., Blanke, A., Doktorowski, S., Ewald, F., et al. (2021). Overview: Fusion of radar polarimetry and numerical atmospheric modelling towards an improved understanding of cloud and precipitation processes. *Atmospheric Chemistry and Physics*, *21*(23), 17291–17314. https://doi.org/10.5194/acp-21-17291-2021

Wolfensberger, D., & Berne, A. (2018). From model to radar variables: A new forward polarimetric radar operator for COSMO. *Atmospheric Measurement Techniques*, *11*(7), 3883–3916. https://doi.org/10.5194/amt-11-3883-2018

Wolfensberger, D., Scipion, D., & Berne, A. (2016). Detection and characterization of the melting layer based on polarimetric radar scans. *Quarterly Journal of the Royal Meteorological Society*, *142*(S1), 108–124. https://doi.org/10.1002/qj.2672

Wu, D., Zhang, F., Chen, X., Ryzhkov, A., Zhao, K., Kumjian, M. R., et al. (2021). Evaluation of microphysics schemes in tropical cyclones using polarimetric radar observations: Convective precipitation in an outer rainband. *Monthly Weather Review*, *149*(4), 1055–1068. https://doi.org/10.1175/mwr-d-19-0378.1

Xie, X., Shrestha, P., Mendrok, J., Carlin, J., Trömel, S., & Blahak, U. (2021). *Bonn polarimetric radar forward operator (B-PRO)* (p. 10). CRC/TR32 Database (TR32DB).

Zeng, Y., Blahak, U., & Jerger, D. (2016). An efficient modular volume-scanning radar forward operator for NWP models: Description and coupling to the COSMO model. *Quarterly Journal of the Royal Meteorological Society*, *142*(701), 3234–3256. https://doi.org/10.1002/qj.2904

Zhang, G. (2016). *Weather radar polarimetry*. CRC Press.

Zhang, G., Gao, J., & Du, M. (2021). Parameterized forward operators for simulation and assimilation of polarimetric radar data with numerical weather predictions. *Advances in Atmospheric Sciences*, *38*(5), 737–754. https://doi.org/10.1007/s00376-021-0289-6

Zhang, G., Mahale, V. N., Putnam, B. J., Qi, Y., Cao, Q., Byrd, A. D., et al. (2019). Current status and future challenges of weather radar polarimetry: Bridging the gap between radar meteorology/hydrology/engineering and numerical weather prediction. *Advances in Atmospheric Sciences*, *36*(6), 571–588. https://doi.org/10.1007/s00376-019-8172-4

Zhang, G., Sun, J., & Brandes, E. A. (2006). Improving parameterization of rain microphysics with disdrometer and radar observations. *Journal of the Atmospheric Sciences*, *63*(4), 1273–1290. https://doi.org/10.1175/JAS3680.1

Zhang, G., Vivekanandan, J., & Brandes, E. (2001). A method for estimating rain rate and drop size distribution from polarimetric radar measurements. *IEEE Transactions on Geoscience and Remote Sensing*, *39*(4), 830–841. https://doi.org/10.1109/36.917906

Zhou, A., Zhao, K., Lee, W.-C., Ding, Z., Lu, Y., & Huang, H. (2022). Evaluation and modification of microphysics schemes on the cold pool evolution for a simulated bow echo in southeast China. *Journal of Geophysical Research: Atmospheres*, *127*(2), e2021JD035262. https://doi.org/10.1029/2021JD035262

Zhu, K., Xue, M., Ouyang, K., & Jung, Y. (2020). Assimilating polarimetric radar data with an ensemble Kalman filter: OSSEs with a tornadic supercell storm simulated with a two-moment microphysics scheme. *Quarterly Journal of the Royal Meteorological Society*, *146*(729), 1880–1900. https://doi.org/10.1002/qj.3772